

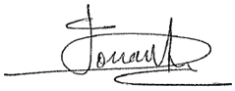




# SEA LEVEL BUDGET CLOSURE - CLIMATE CHANGE INITIATIVE +

## ALGORITHM THEORETICAL BASELINE DOCUMENT

	Name	Organisation	Date	Visa
Written by :	Martin Horwath Thorben Döhne	TU Dresden	31/03/2025	
	Anne Barnoud Robin Fraudeau Marie Bouih	Magellium		
	Rémy Asselot William Llovel Nicolas Kolodziejczyk Kevin Balem	LOPS		
	Hugo Lecomte Benoit Meyssignac Anny Cazenave Alejandro Blazquez Sébastien Fourest	LEGOS		
	Jonathan Bamber Anrijs Abele Xueqing Yin	Univ. Bristol		
	Giorgio Spada	UNIBO		
	Stéphanie Leroux	Datlas		

Checked by :	Michaël Ablain	Magellium	31/03/2025	
Approved by :	Joël Dorandeu	Magellium	31/03/2025	
Accepted by :	Sarah Connors	ESA		

Document reference:	SLBC_CCI-DT-041-MAG_ABD_D2-4
Edition.Revision:	2.0
Release date:	31/03/2025
Customer:	ESA
Ref. Market, consultation:	ESA AO/1-11340/22/I-NB



### Mailing list

	Name	organisation	Nb. copies
Recipients :	Sarah Connors Marco Restano	ESA	1 digital copy
Internal copy :			1 digital copy

### Document evolution sheet

Ed.	Rev.	Date	Purpose of evolution	Observations
1	0	31/10/2024	First version of the document	
1	1	15/11/2024	ESA review	
2	0	31/03/2025	Update of the document	Modifications on the Algorithm paragraph



## Contents

<b>1. Introduction</b>	<b>10</b>
1.1. Purpose of document	10
1.2. Document structure	10
1.3. Related documents	11
1.3.1. Applicable documents	11
1.3.2. Bibliography	11
1.4. Acronyms	11
<b>2. Input data products</b>	<b>13</b>
2.1. Absolute sea level	13
2.1.1. Review of scientific background	13
2.1.2. Selection of used data	13
2.1.3. Algorithms	13
2.1.4. Uncertainty assessment	14
2.1.5. Known limitations	15
2.2. Steric sea level	16
2.2.1. Review of scientific background	16
2.2.2. Selection of used data	16
2.2.3. Algorithms	17
2.2.4. Uncertainty assessment	17
2.2.5. Known limitations	17
2.3. Ocean mass from space gravimetry	18
2.3.1. Review of scientific background	18
2.3.2. Selection of used data	18
2.3.3. Algorithms	19
2.3.4. Uncertainty assessment	22
2.3.5. Known limitations	24
2.4. Ocean mass from land and atmosphere components: Greenland Ice Sheet	25
2.4.1. Review of scientific background	25
2.4.2. Selection of used data	25
2.4.3. Algorithms	26
2.4.4. Uncertainty assessment	26
2.4.5. Known limitations	27
2.5. Ocean mass from land and atmosphere components: Antarctic Ice Sheet	28
2.5.1. Review of scientific background	28
2.5.2. Selection of used data	28
2.5.3. Algorithms	28
2.5.4. Uncertainty assessment	28
2.5.5. Known limitations	28
2.6. Ocean mass from land and atmosphere components: Glaciers and ice caps	28

2.6.1. Review of scientific background	28
2.6.2. Selection of used data	29
2.6.3. Algorithms	32
2.6.4. Uncertainty assessment	32
2.6.5. Known limitations	32
2.7. Ocean mass from land and atmosphere components: Land water storage	32
2.7.1. Review of scientific background	32
2.7.2. Selection of used data	34
2.7.3. Algorithms	35
2.7.4. Uncertainty assessment	35
2.7.5. Known limitations	36
2.8. Ocean mass from land and atmosphere components: Atmosphere water vapour	38
2.8.1. Review of scientific background	38
2.8.2. Selection of used data	38
2.8.3. Algorithms	39
2.8.4. Uncertainty assessment	39
2.8.5. Known limitations	40
2.9. Fingerprints and GIA	40
2.9.1. Selection of used data	41
2.9.2. Algorithms	41
2.9.3. Uncertainty assessment	41
2.9.4. Known limitations	41
2.10. Synthetic observations	1
2.10.1. Review of scientific background	1
2.10.2. Selection of used data	1
2.10.2.1. Altimetric synthetic data	1
2.10.2.2. Temperature and salinity synthetic data	1
2.10.2.3. Gravimetric synthetic data	1
2.10.3. Algorithms	1
2.10.3.1. Altimetric synthetic data	1
2.10.3.2. Steric synthetic data	1
2.10.3.3. Gravimetric synthetic data	1
2.10.4. Known limitations	1
2.10.4.1. Altimetric synthetic data	1
2.10.4.2. Steric synthetic data	1
2.10.4.3. Gravimetric synthetic data	1
<b>3. Sea level budget computation chain</b>	<b>1</b>
3.1. Overview	1
3.2. Input data	1
3.3. Sea level budget and Ocean mass budget equations	1

3.4. Algorithms	1
3.4.1. Unconstrained approach: Historical approach	1
3.4.1.1. Computation of the sea level budget residuals	1
3.4.1.2. Computation of the global mean sea level budget residuals	1
3.4.2. Constrained approach: Innovative approach	1
3.4.2.1. Estimation of global mean components	1
3.4.2.2. Estimation of global mean components with ocean mass balance estimates	1
3.4.2.3. Estimation of local sea level budget components	1
3.5. Known limitations	1

## List of tables

Table 1: List of applicable documents.	11
Table 2: List of acronyms.	16
Table 3: Sources of uncertainties of the global mean sea level and their estimates, adapted from Guérou et al. (2023). Values in bold font have been updated since the estimates published by Guérou et al. (2023). In gray, the GIA contribution to sea level uncertainty is not applicable to the component not corrected for the GIA effect as described in this section, but this uncertainty contribution may be considered for any separate GIA component.	18
Table 4: Sources of uncertainties of the sea level change and their estimates, from Prandi et al. (2021). Location dependent standard uncertainties are provided in the Prandi et al. (2020) dataset. In gray, the GIA contribution to sea level uncertainty is not applicable to the component not corrected for the GIA effect as described in this section, but this uncertainty contribution may be considered for any separate GIA component.	19

## List of figures

Figure 1: Scope of the Product Specification Document (PSD), Data Access Requirement Document (DARD) and Algorithm Theoretical Baseline Document (ATBD).	11
Figure 2: mean linear trend of surface mass distribution from satellite gravimetry over 2002-04 – 2023-12, from the Level-2 based mascon solution developed at TU Dresden.	25
Figure 3: mass change of the global ocean, expressed in barystatic sea level, from the following satellite-gravity based solutions (see legend): L2-based mascon solution by TU Dresden (TUD MSCN, black) and L1-based mascon solutions by JPL (blue), CSR (orange), GSFC (green). Mean linear trends are quoted in the legend.	26
Figure 4: Temporal error covariance matrix of the time series of global ocean mass anomalies corresponding to the TU Dresden L2-based mascon solution. The axis shows sequential numbers of the monthly solutions, irrespective of temporal gaps (most notably the GRACE – GRACE-FO gap between No. 162 and 163).	27
Figure 5: Ice sheet (blue) and the 19 GIC sectors (yellow) that are part of the mass exchange estimates provided for land ice. The size of the circles represents the	33

glaciated area and the percentage that is blue or green represents how much of the area is marine terminating or land terminating respectively.

Figure 6: Illustration of the methodology (From (Dussaillant et al., 2024); a) illustrates the search area around the glacier where in situ observations exist that overlap with the ASTER data, b) shows the time series for the 10 glaciers in the search area, c) shows the geodetic data for the glacier used to calibrate the in-situ data and d) is the new calibrated time series for the glacier with uncertainties. 34

Figure 7 The mass balance time series at annual time resolution for all 19 sectors, alongside the 2-sigma uncertainties. Calibrated mass balance times series for all 19 GIC sectors. The area of the pie charts represents the mass lost since 1976 and the coloured region the mass loss from 2014-2023. 35

Figure 8: Comparison of the estimate of land water storage variation contribution to sea level change from various hydrological models: four estimates of the WaterGAP Hydrological Model (WGHM) version 22e, the ISBA-CTRIP hydrological model and six estimates of the GRACE\_REC model. Plain lines indicate estimates including the human-induced contribution ("hum.") while dotted lines indicate estimates taking into consideration only the climate-driven contribution ("cli."). Only the GRACE-REC estimates include the land ice contribution. 37

Figure 9: Land water storage variations contribution to global mean sea level change, from the WaterGap Hydrological Model (WGHM) version 22e using ERA5 climate forcing and including the anthropogenic contribution. 38

Figure 10: Construction of ensemble of the estimate of the land water storage contribution uncertainty, using four WGHM 22e datasets. (a) WGHM 22e LWS contributions to global mean sea level with ERA5 and W5E5 climate forcing, with and without taking into account the anthropogenic contribution. (b) The anthropogenic contribution estimated from the differences between the two ERA5-forced timeseries is added to the timeseries without anthropogenic contribution. (c) Detrended time series. 40

Figure 11: Standard uncertainties of the land water storage contribution component. The blue curve results from the standard deviation of the ensemble of detrended estimates (see Figure 10c). The green curve accounts for the trend uncertainties for the climate-driven and human-induced contributions provided by Cáceres et al. (2020). The orange curve is the resulting combined standard uncertainty. 41

Figure 12: Atmosphere water vapour content change contribution to global mean sea level change, computed from ERA5 total column water vapour data. 42

Figure 13: Comparison of the atmosphere water vapour contribution estimated from ERA5 and from the sum of the ESA CCI water vapour data over land and of the 43



HOAPS water vapour data over the oceans. (a) Time series. (b) Time series difference.

Figure 14: Elastic fingerprints due to trends of present-day mass redistribution on sea surface height change ( $dN/dt$ ). These rates are obtained as a least-squares linear fit of the monthly time series for each field, from April 2002 to December 2019. 45

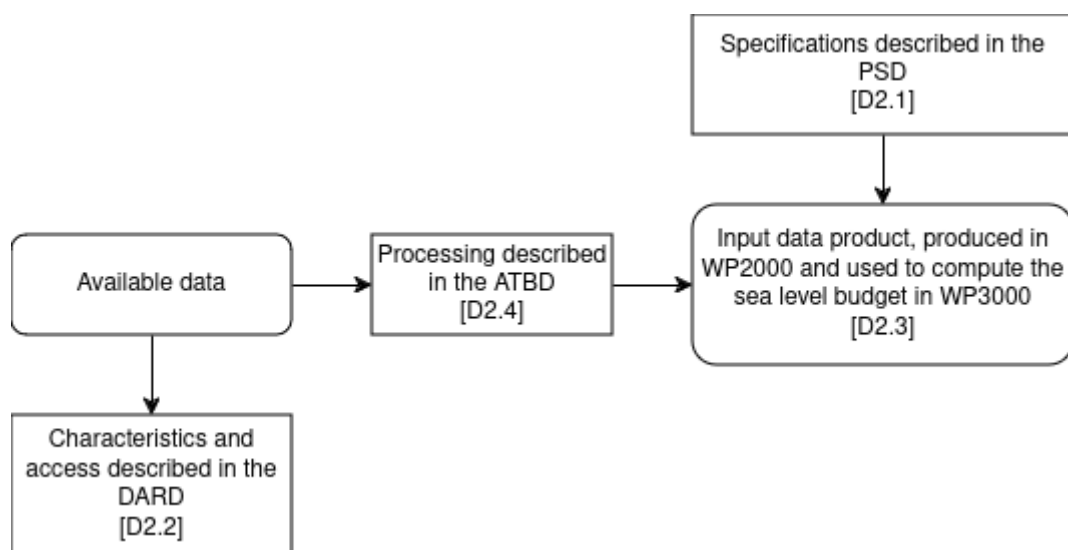
Figure 15: GIA contribution to the present-day rate of absolute sea-level change ( $dN/dt$ , left), according to the ICE-6G (VM5a) model of Argus et al. (2014) and Peltier et al. (2015), implemented into the Sea Level Equation solver SELEN4, and associated uncertainties (right) evaluated as ensemble standard deviations over 20 variations of the VM5a rheological profile. These rates are representative of the time period from April 2002 to December 2019. 45

Figure 16: Workflow of the gravimetric synthetic data processing 49

# 1. Introduction

## 1.1. Purpose of document

This document is the Algorithm Theoretical Baseline Document (ATBD) for the ESA SLBC\_cci+ project ([AD-1] and [AD-2]). This ATBD is dedicated to the description and justification of the algorithms used in the generation of the SLBC product. It contains the description of the processing of the components, from the available data described in the Data Access Requirement Document (DARD) [AD-5] to the input data product [D2.3] used to compute the sea level budget, following the specifications prescribed in the Product Specification Document (PSD) [AD-4]. It also contains the algorithms for the computation of the sea level budget. Fig.1 summarises the content and scope of the Product Specification Document (PSD), Data Access Requirement Document (DARD) and Algorithm Theoretical Baseline Document (ATBD).



*Figure 1: Scope of the Product Specification Document (PSD), Data Access Requirement Document (DARD) and Algorithm Theoretical Baseline Document (ATBD).*

## 1.2. Document structure

In addition to this introduction, this document includes the following sections:

- Section 2 describes the components of the input data product and their processing,
- Section 3 provides the algorithms for the computation of the sea level budget.

## 1.3. Related documents

### 1.3.1. Applicable documents

*Table 1: List of applicable documents.*

Id.	Ref.	Description
[AD-1]	ESA AO/1-11340/22/I-NB	Call to tender “SEA LEVEL BUDGET CLOSURE_CCI+ (SLBC_CCI+)”
[AD-2]	MAG-22-PTF-060_Detailed Proposal_V2	Detailed proposal in response to ESA/ESRIN Request for Quotation “SEA LEVEL BUDGET CLOSURE_CCI+ (SLBC_CCI+)” ESA AO/1-11340/22/I-NB [AD-1]
[AD-3]	SLBC_CCI-DT-008-MAG_S RD_D1-1	SEA LEVEL BUDGET CLOSURE_CCI+ Science Requirements Document Version 1.2, 07/06/2024
[AD-4]	SLBC_CCI-DT-039-MAG_P SD_D2-1	SEA LEVEL BUDGET CLOSURE_CCI+ Product Specification Document
[AD-5]	SLBC_CCI-DT-040-MAG_D ARD_D2-2	SEA LEVEL BUDGET CLOSURE_CCI+ Data Access Requirement Document (DARD)

### 1.3.2. Bibliography

- Ablain, M., Meyssignac, B., Zawadzki, L., Jugier, R., Ribes, A., Spada, G., Benveniste, J., Cazenave, A., and Picot, N.: Uncertainty in satellite estimates of global mean sea-level changes, trend and acceleration, *Earth Syst. Sci. Data*, 11, 1189–1202, <https://doi.org/10.5194/essd-11-1189-2019>, 2019.
- Argus, D. F., Peltier, W. R., Drummond, R., and Moore, A. W.: The Antarctica component of postglacial rebound model ICE-6G\_C (VM5a) based on GPS positioning, exposure age dating of ice thicknesses, and relative sea level histories, *Geophys. J. Int.*, 198, 537–563, <https://doi.org/10.1093/gji/ggu140>, 2014.
- Bamber, J. L., Westaway, R. M., Marzeion, B., and Wouters, B.: The land ice contribution to sea level during the satellite era, *Environ. Res. Lett.*, 13, 063008, <https://doi.org/10.1088/1748-9326/aac2f0>, 2018.
- Barnoud, A., Pfeffer, J., Guérou, A., Frery, M., Siméon, M., Cazenave, A., Chen, J., Llovel, W., Thierry, V., Legeais, J., and Ablain, M.: Contributions of Altimetry and Argo to Non-Closure of the Global Mean Sea Level Budget Since 2016, *Geophys. Res. Lett.*, 48, e2021GL092824, <https://doi.org/10.1029/2021GL092824>, 2021.
- Barnoud, A., Pfeffer, J., Cazenave, A., Fraudeau, R., Rousseau, V., and Ablain, M.: Revisiting the global mean ocean mass budget over 2005–2020, *Ocean Sci.*, 19, 321–334, <https://doi.org/10.5194/os-19-321-2023>, 2023.
- Bergmann-Wolf, I., Zhang, L., and Dobslaw, H.: Global Eustatic Sea-Level Variations for the Approximation of Geocenter Motion from Grace, *J. Geod. Sci.*, 4, <https://doi.org/10.2478/jogs-2014-0006>, 2014.

- Bessi res, L., Leroux, S., Brankart, J.-M., Molines, J.-M., Moine, M.-P., Bouttier, P.-A., Penduff, T., Terray, L., Barnier, B., and S razin, G.: Development of a probabilistic ocean modelling system based on NEMO 3.5: application at eddying resolution, *Geosci. Model Dev.*, 10, 1091–1106, <https://doi.org/10.5194/gmd-10-1091-2017>, 2017.
- Blazquez, A., Meyssignac, B., Lemoine, J., Berthier, E., Ribes, A., and Cazenave, A.: Exploring the uncertainty in GRACE estimates of the mass redistributions at the Earth surface: implications for the global water and sea level budgets, *Geophys. J. Int.*, 215, 415–430, <https://doi.org/10.1093/gji/ggy293>, 2018.
- Bretherton, F. P., Davis, R. E., and Fandry, C. B.: A technique for objective analysis and design of oceanographic experiments applied to MODE-73, *Deep Sea Res. Oceanogr. Abstr.*, 23, 559–582, [https://doi.org/10.1016/0011-7471\(76\)90001-2](https://doi.org/10.1016/0011-7471(76)90001-2), 1976.
- Brown, S., Willis, J., and Fournier, S.: Jason-3 Wet Path Delay Correction (Ver. F. PO.DAAC), <https://doi.org/10.5067/J3L2G-PDCOR>, 2023.
- C ceres, D., Marzeion, B., Malles, J. H., Gutknecht, B. D., Schmied, H. M., and D ll, P.: Assessing global water mass transfers from continents to oceans over the period 1948–2016, *Hydrol. Earth Syst. Sci.*, 24, 4831–4851, <https://doi.org/10.5194/hess-24-4831-2020>, 2020.
- Caron, L., Ivins, E. R., Larour, E., Adhikari, S., Nilsson, J., and Blewitt, G.: GIA Model Statistics for GRACE Hydrology, Cryosphere, and Ocean Science, *Geophys. Res. Lett.*, 45, 2203–2212, <https://doi.org/10.1002/2017GL076644>, 2018.
- Chambers, D. P., Cazenave, A., Champollion, N., Dieng, H., Llovel, W., Forsberg, R., von Schuckmann, K., and Wada, Y.: Evaluation of the Global Mean Sea Level Budget between 1993 and 2014, *Surv. Geophys.*, 38, 309–327, <https://doi.org/10.1007/s10712-016-9381-3>, 2017.
- Copernicus Climate Change Service, C. D. S.: Sea level daily gridded data from satellite observations for the global ocean from 1993 to present, <https://doi.org/10.24381/CDS.4C328C78>, 2018.
- Croteau, M. J., Sabaka, T. J., and Loomis, B. D.: GRACE Fast Mascons From Spherical Harmonics and a Regularization Design Trade Study, *J. Geophys. Res. Solid Earth*, 126, <https://doi.org/10.1029/2021JB022113>, 2021.
- Decharme, B., Delire, C., Minvielle, M., Colin, J., Vergnes, J.-P., Alias, A., Saint-Martin, D., S f rian, R., S n si, S., and Voldoire, A.: Recent Changes in the ISBA-CTRIP Land Surface System for Use in the CNRM-CM6 Climate Model and in Global Off-Line Hydrological Applications, *J. Adv. Model. Earth Syst.*, 11, 1207–1252, <https://doi.org/10.1029/2018ms001545>, 2019.
- Dieng, H. B., Cazenave, A., Meyssignac, B., and Ablain, M.: New estimate of the current rate of sea level rise from a sea level budget approach, *Geophys. Res. Lett.*, 44, 3744–3751, <https://doi.org/10.1002/2017gl073308>, 2017.
- Ditmar, P.: Conversion of time-varying Stokes coefficients into mass anomalies at the Earth’s surface considering the Earth’s oblateness, *J. Geod.*, 92, 1401–1412, <https://doi.org/10.1007/s00190-018-1128-0>, 2018.
- Ditmar, P.: How to quantify the accuracy of mass anomaly time-series based on GRACE data in the absence of knowledge about true signal?, *J. Geod.*, 96, 54, <https://doi.org/10.1007/s00190-022-01640-x>, 2022.
- D hne, T., Horwath, M., Groh, A., and Buchta, E.: The sensitivity kernel perspective on GRACE mass change estimates, *J. Geod.*, 97, 11, <https://doi.org/10.1007/s00190-022-01697-8>, 2023.
- Dussailant, I., Hugonnet, R., Huss, M., Berthier, E., Bannwart, J., Paul, F., and Zemp, M.: Annual mass changes for each glacier in the world from 1976 to 2023, *Earth Syst. Sci. Data Discuss.*, 1–41, <https://doi.org/10.5194/essd-2024-323>, 2024.

- Dussin, R., Barnier, B., Brodeau, L., and Molines, J.-M.: The making of the DRAKKAR forcing set DFS5, 2016.
- Farrell, W. E. and Clark, J. A.: On Postglacial Sea Level, *Geophys. J. R. Astron. Soc.*, 46, 647–667, <https://doi.org/10.1111/j.1365-246x.1976.tb01252.x>, 1976.
- Gaillard, F., Reynaud, T., Thierry, V., Kolodziejczyk, N., and Schuckmann, K. von: In Situ–Based Reanalysis of the Global Ocean Temperature and Salinity with ISAS: Variability of the Heat Content and Steric Height, *J. Clim.*, 29, 1305–1323, <https://doi.org/10.1175/JCLI-D-15-0028.1>, 2016.
- Good, S. A., Martin, M. J., and Rayner, N. A.: EN4: Quality controlled ocean temperature and salinity profiles and monthly objective analyses with uncertainty estimates, *J. Geophys. Res. Oceans*, 118, 6704–6716, <https://doi.org/10.1002/2013JC009067>, 2013.
- Gregory, J. M. and Lowe, J. A.: Predictions of global and regional sea-level rise using AOGCMs with and without flux adjustment, *Geophys. Res. Lett.*, 27, 3069–3072, <https://doi.org/10.1029/1999GL011228>, 2000.
- Gregory, J. M., Griffies, S. M., Hughes, C. W., Lowe, J. A., Church, J. A., Fukimori, I., Gomez, N., Kopp, R. E., Landerer, F., Cozannet, G. L., Ponte, R. M., Stammer, D., Tamisiea, M. E., and van de Wal, R. S. W.: Concepts and Terminology for Sea Level: Mean, Variability and Change, Both Local and Global, *Surv. Geophys.*, 40, 1251–1289, <https://doi.org/10.1007/s10712-019-09525-z>, 2019.
- Groh, A. and Horwath, M.: Antarctic Ice Mass Change Products from GRACE/GRACE-FO Using Tailored Sensitivity Kernels, *Remote Sens.*, 13, 1736, <https://doi.org/10.3390/rs13091736>, 2021.
- Groh, A., Buchta, E., Horwath, M., Willen, M. O., Döhne, T., Gutknecht, B. D., and Kappelsberger, M. T.: Temporal error covariances of satellite gravimetry-derived ice mass change products, 2021.
- Guérou, A., Meyssignac, B., Prandi, P., Ablain, M., Ribes, A., and Bignalet-Cazalet, F.: Current observed global mean sea level rise and acceleration estimated from satellite altimetry and the associated measurement uncertainty, *Ocean Sci.*, 19, 431–451, <https://doi.org/10.5194/os-19-431-2023>, 2023.
- Horwath, M., Gutknecht, B. D., Cazenave, A., Palanisamy, H. K., Marti, F., Marzeion, B., Paul, F., Bris, R. L., Hogg, A. E., Otsuka, I., Shepherd, A., Döll, P., Cáceres, D., Schmied, H. M., Johannessen, J. A., Nilsen, J. E. Ø., Raj, R. P., Forsberg, R., Sørensen, L. S., Barletta, V. R., Simonsen, S. B., Knudsen, P., Andersen, O. B., Randall, H., Rose, S. K., Merchant, C. J., Macintosh, C. R., Schuckmann, K. von, Novotny, K., Groh, A., Restano, M., and Benveniste, J.: Global sea-level budget and ocean-mass budget, with focus on advanced data products and uncertainty characterisation, *Earth Syst. Sci. Data*, 14, 411–447, <https://doi.org/10.5194/essd-14-411-2022>, 2022.
- Hugonnet, R., McNabb, R., Berthier, E., Menounos, B., Nuth, C., Girod, L., Farinotti, D., Huss, M., Dussaillant, I., Brun, F., and Kääb, A.: Accelerated global glacier mass loss in the early twenty-first century, *Nature*, 592, 726–731, <https://doi.org/10.1038/s41586-021-03436-z>, 2021.
- Humphrey, V. and Gudmundsson, L.: GRACE-REC: a reconstruction of climate-driven water storage changes over the last century, *Earth Syst. Sci. Data*, 11, 1153–1170, <https://doi.org/10.5194/essd-11-1153-2019>, 2019.
- Ingleby, B. and Huddleston, M.: Quality control of ocean temperature and salinity profiles — Historical and real-time data, *J. Mar. Syst.*, 65, 158–175, <https://doi.org/10.1016/j.jmarsys.2005.11.019>, 2007.
- Ivins, E. R., James, T. S., Wahr, J., O. Schrama, E. J., Landerer, F. W., and Simon, K. M.: Antarctic contribution to sea level rise observed by GRACE with improved GIA correction, *J. Geophys. Res. Solid Earth*, 118, 3126–3141, <https://doi.org/10.1002/jgrb.50208>, 2013.

- Kolodziejczyk, N., Prigent-Mazella, A., and Gaillard, F.: ISAS temperature, salinity, dissolved oxygen gridded fields, <https://doi.org/10.17882/52367>, 2023.
- Kustowski, B., Ekström, G., and Dziewoński, A. M.: Anisotropic shear-wave velocity structure of the Earth's mantle: A global model, *J. Geophys. Res. Solid Earth*, 113, 2007JB005169, <https://doi.org/10.1029/2007JB005169>, 2008.
- Kvas, A., Behzadpour, S., Ellmer, M., Klinger, B., Strasser, S., Zehentner, N., and Mayer-Gürr, T.: ITSG-Grace2018: Overview and Evaluation of a New GRACE-Only Gravity Field Time Series, *J. Geophys. Res. Solid Earth*, 124, 9332–9344, <https://doi.org/10.1029/2019JB017415>, 2019.
- Landerer, F. W., Flechtner, F. M., Save, H., Webb, F. H., Bandikova, T., Bertiger, W. I., Bettadpur, S. V., Byun, S. H., Dahle, C., Dobslaw, H., Fahnestock, E., Harvey, N., Kang, Z., Kruizinga, G. L. H., Loomis, B. D., McCullough, C., Murböck, M., Nagel, P., Paik, M., Pie, N., Poole, S., Strelak, D., Tamisiea, M. E., Wang, F., Watkins, M. M., Wen, H.-Y., Wiese, D. N., and Yuan, D.-N.: Extending the Global Mass Change Data Record: GRACE Follow-On Instrument and Science Data Performance, *Geophys. Res. Lett.*, 47, e2020GL088306, <https://doi.org/10.1029/2020GL088306>, 2020.
- L'Ecuyer, T. S., Beaudoin, H. K., Rodell, M., Olson, W., Lin, B., Kato, S., Clayson, C. A., Wood, E., Sheffield, J., Adler, R., Huffman, G., Bosilovich, M., Gu, G., Robertson, F., Houser, P. R., Chambers, D., Famiglietti, J. S., Fetzer, E., Liu, W. T., Gao, X., Schlosser, C. A., Clark, E., Lettenmaier, D. P., and Hilburn, K.: The Observed State of the Energy Budget in the Early Twenty-First Century, *J. Clim.*, 28, 8319–8346, <https://doi.org/10.1175/JCLI-D-14-00556.1>, 2015.
- Llovel, W., Purkey, S., Meyssignac, B., Blazquez, A., Kolodziejczyk, N., and Bamber, J.: Global ocean freshening, ocean mass increase and global mean sea level rise over 2005–2015, *Sci. Rep.*, 9, 17717, <https://doi.org/10.1038/s41598-019-54239-2>, 2019.
- Llovel, W., Kolodziejczyk, N., Close, S., Penduff, T., Molines, J.-M., and Terray, L.: Imprint of intrinsic ocean variability on decadal trends of regional sea level and ocean heat content using synthetic profiles, *Environ. Res. Lett.*, 17, 044063, <https://doi.org/10.1088/1748-9326/ac5f93>, 2022.
- Loomis, B. D., Luthcke, S. B., and Sabaka, T. J.: Regularization and error characterization of GRACE mascons, *J. Geod.*, 93, 1381–1398, <https://doi.org/10.1007/s00190-019-01252-y>, 2019.
- Marzeion, B., Jarosch, A. H., and Hofer, M.: Past and future sea-level change from the surface mass balance of glaciers, *The Cryosphere*, 6, 1295–1322, <https://doi.org/10.5194/tc-6-1295-2012>, 2012.
- Marzeion, B., Leclercq, P. W., Cogley, J. G., and Jarosch, A. H.: Brief Communication: Global reconstructions of glacier mass change during the 20th century are consistent, *The Cryosphere*, 9, 2399–2404, <https://doi.org/10.5194/tc-9-2399-2015>, 2015.
- Meyer, U.: COST-G RL01 Release Notes, 19, 2020.
- Meyer, U., Lasser, M., Dahle, C., Förste, C., Behzadpour, S., Koch, I., and Jäggi, A.: Combined monthly GRACE-FO gravity fields for a Global Gravity-based Groundwater Product, *Geophys. J. Int.*, 236, 456–469, <https://doi.org/10.1093/gji/ggad437>, 2024.
- Müller Schmied, H., Trautmann, T., Ackermann, S., Cáceres, D., Flörke, M., Gerdener, H., Kynast, E., Peiris, T. A., Schiebener, L., Schumacher, M., and Döll, P.: The global water resources and use model WaterGAP v2.2e: description and evaluation of modifications and new features, <https://doi.org/10.5194/gmd-2023-213>, 20 November 2023.
- Ohtsuka, I. N., Shepherd, A., Ivins, E. R., Schlegel, N.-J., Amory, C., van den Broeke, M. R., Horwath, M., Joughin, I., King, M. D., Krinner, G., Nowicki, S., Payne, A. J., Rignot, E., Scambos, T., Simon, K. M., Smith, B. E., Sørensen, L. S., Velicogna, I., Whitehouse, P. L., A. G., Agosta, C., Ahlstrøm, A. P., Blazquez, A., Colgan, W., Engdahl, M. E., Fettweis, X.,



- Forsberg, R., Gallée, H., Gardner, A., Gilbert, L., Gourmelen, N., Groh, A., Gunter, B. C., Harig, C., Helm, V., Khan, S. A., Kittel, C., Konrad, H., Langen, P. L., Lecavalier, B. S., Liang, C.-C., Loomis, B. D., McMillan, M., Melini, D., Mernild, S. H., Mottram, R., Mouginot, J., Nilsson, J., Noël, B., Pattle, M. E., Peltier, W. R., Pie, N., Roca, M., Sasgen, I., Save, H. V., Seo, K.-W., Scheuchl, B., Schrama, E. J. O., Schröder, L., Simonsen, S. B., Slater, T., Spada, G., Sutterley, T. C., Vishwakarma, B. D., van Wessem, J. M., Wiese, D., van der Wal, W., and Wouters, B.: Mass balance of the Greenland and Antarctic ice sheets from 1992 to 2020, *Earth Syst. Sci. Data*, 15, 1597–1616, <https://doi.org/10.5194/essd-15-1597-2023>, 2023a.
- Ootosaka, I. N., Horwath, M., Mottram, R., and Nowicki, S.: Mass Balances of the Antarctic and Greenland Ice Sheets Monitored from Space, *Surv. Geophys.*, 44, 1615–1652, <https://doi.org/10.1007/s10712-023-09795-8>, 2023b.
  - Peltier, W. R., Argus, D. F., and Drummond, R.: Space geodesy constrains ice age terminal deglaciation: The global ICE-6G\_C (VM5a) model, *J. Geophys. Res. Solid Earth*, 120, 450–487, <https://doi.org/10.1002/2014JB011176>, 2015.
  - Peltier, W. R., Argus, D. F., and Drummond, R.: Comment on “An Assessment of the ICE-6G\_C (VM5a) Glacial Isostatic Adjustment Model” by Purcell et al., *J. Geophys. Res. Solid Earth*, 123, 2019–2028, <https://doi.org/10.1002/2016JB013844>, 2018.
  - Prandi, P., Meyssignac, B., Ablain, M., Spada, G., and Ribes, A.: Error variance-covariance, trends, accelerations and uncertainties of regional mean sea level estimated from satellite altimetry, <https://doi.org/10.17882/74862>, 2020.
  - Prandi, P., Meyssignac, B., Ablain, M., Spada, G., Ribes, A., and Benveniste, J.: Local sea level trends, accelerations and uncertainties over 1993–2019, *Sci. Data*, 8, 1, <https://doi.org/10.1038/s41597-020-00786-7>, 2021.
  - Rodell, M., Beaudoin, H., L’Ecuyer, T., Olson, W., Famiglietti, J., Houser, P., Adler, R., Bosilovich, M., Clayson, C., Chambers, D., Clark, E., Fetzer, E., Gu, G., Hilburn, K., Huffman, G., Lettenmaier, D., Liu, W. T. L., Robertson, F., Sheffield, J., and Gao, X.: The Observed State of the Water Cycle in the Early Twenty-First Century, 2015.
  - Roy, K. and Peltier, W. R.: Glacial isostatic adjustment, relative sea level history and mantle viscosity: reconciling relative sea level model predictions for the U.S. East coast with geological constraints, *Geophys. J. Int.*, 201, 1156–1181, <https://doi.org/10.1093/gji/ggv066>, 2015.
  - Save, H., Bettadpur, S., and Tapley, B. D.: High-resolution CSR GRACE RL05 mascons, *J. Geophys. Res. Solid Earth*, 121, 7547–7569, <https://doi.org/10.1002/2016jb013007>, 2016.
  - Spada, G. and Melini, D.: SELEN<sup>4</sup> (SELEN version 4.0): a Fortran program for solving the gravitationally and topographically self-consistent sea-level equation in glacial isostatic adjustment modeling, *Geosci. Model Dev.*, 12, 5055–5075, <https://doi.org/10.5194/gmd-12-5055-2019>, 2019.
  - Sun, Y., Riva, R., and Ditmar, P.: Optimizing estimates of annual variations and trends in geocenter motion and J2 from a combination of GRACE data and geophysical models, *J. Geophys. Res. Solid Earth*, 121, 8352–8370, <https://doi.org/10.1002/2016JB013073>, 2016.
  - Swenson, S., Chambers, D., and Wahr, J.: Estimating geocenter variations from a combination of GRACE and ocean model output, *J. Geophys. Res. Solid Earth*, 113, <https://doi.org/10.1029/2007JB005338>, 2008.
  - Tapley, B. D., Watkins, M. M., Flechtner, F., Reigber, C., Bettadpur, S., Rodell, M., Sasgen, I., Famiglietti, J. S., Landerer, F. W., Chambers, D. P., Reager, J. T., Gardner, A. S., Save, H., Ivins, E. R., Swenson, S. C., Boening, C., Dahle, C., Wiese, D. N., Dotslaw, H., Tamisiea, M. E., and Velicogna, I.: Contributions of GRACE to understanding climate change, *Nat. Clim. Change*, 9, 358–369, <https://doi.org/10.1038/s41558-019-0456-2>, 2019.
  - Uebbing, B., Kusche, J., Rietbroek, R., and Landerer, F. W.: Processing Choices Affect

- Ocean Mass Estimates From GRACE, J. Geophys. Res. Oceans, 124, 1029–1044, <https://doi.org/10.1029/2018JC014341>, 2019.
- WCRP Global Sea Level Budget Group: Global sea-level budget 1993–present, Earth Syst. Sci. Data, 10, 1551–1590, <https://doi.org/10.5194/essd-10-1551-2018>, 2018.
  - Wiese, D. N., Landerer, F. W., and Watkins, M. M.: Quantifying and reducing leakage errors in the JPL RL05M GRACE mascon solution, Water Resour. Res., 52, 7490–7502, <https://doi.org/10.1002/2016WR019344>, 2016.
  - Wouters, B., Gardner, A. S., and Moholdt, G.: Global Glacier Mass Loss During the GRACE Satellite Mission (2002–2016), Front. Earth Sci., 7, <https://doi.org/10.3389/feart.2019.00096>, 2019.
  - Zemp, M. and Welty, E.: Temporal downscaling of glaciological mass balance using seasonal observations, J. Glaciol., 1–6, <https://doi.org/10.1017/jog.2023.66>, 2023.

## 1.4. Acronyms

The list of acronyms that are used in the document is presented in Table 2.

*Table 2: List of acronyms.*

Acronym	Description
C3S	Copernicus Climate Change Service
CCI	The ESA Climate Change Initiative
CDS	Climate Data Store
ECV	Essential Climate Variable
ERA5	ECMWF Atmospheric Reanalysis v5
ESA	European Space Agency
ECMWF	European Centre for Medium-range Weather Forecasts
GIA	Glacial Isostatic Adjustment
HOAPS	Hambourg Ocean-Atmosphere Fluxes and Parameters from Satellite
ISBA-CTRIP	Interaction Soil-Biosphere-Atmosphere, Total Runoff Integrating Pathways from the Centre National de Recherches Météorologiques



LWS	Land Water Storage
SLBC	Sea level budget closure
SLBC_cci	Sea Level Budget Closure of the ESA Climate Change Initiative (first phase)
SLBC_cci+	Sea Level Budget Closure of the ESA Climate Change Initiative (second phase, this activity)
SL_cci	The Sea Level component of the ESA Climate Change Initiative
TCWV	Total Column Water Vapour
TWS	Terrestrial Water Storage
WaterGAP	Water Global Assessment and Prognosis
WGHM	WaterGAP Hydrological Model
w.r.t	With respect to
WTC	Wet Troposphere Correction

## 2. Input data products

### 2.1. Absolute sea level

#### 2.1.1. Review of scientific background

The Copernicus Climate Change Service (C3S) provides altimetry-based sea level anomaly data for climate studies. To ensure long term stability, two missions are used simultaneously at each time as a baseline reference: the current reference mission (TOPEX/Poseidon, Jason-1, Jason-2, Jason-3 and Sentinel-6 Michael Freilich) and an auxiliary mission from the constellation.

## 2.1.2. Selection of used data

The absolute sea level component is computed using the daily gridded Copernicus Climate Change Service (C3S) Climate Data Store (CDS) sea level anomaly dataset (Copernicus Climate Change Service, 2018). This dataset provides the correction to be applied to correct for the drift of the TOPEX-A altimeter. The drift for the Jason-3 wet troposphere correction (WTC) is corrected using the file provided by Brown et al. (2023).

## 2.1.3. Algorithms

The absolute sea level component is computed as follows:

- The daily sea surface height above mean sea level and the TOPEX-A correction variables are aggregated monthly by average over each month.
- The sea surface height above mean sea level and the TOPEX-A correction variables are downsampled from  $0.25^\circ \times 0.25^\circ$  to  $1^\circ \times 1^\circ$  with spatial means weighted by the ocean surface within each cell.
- The TOPEX-A drift correction is removed from the sea surface height above mean sea level.
- The Jason-3 WTC correction, provided for each altimetry path, is interpolated along altimetry tracks and processed following the AVISO procedure of computation of the gridded and global mean sea level: aggregation of along-track data in  $3^\circ \times 1^\circ$  grids, and global mean computation. The Jason-3 WTC correction is applied homogeneously everywhere.
- The Jason-3 WTC correction is removed from the sea surface height corrected for the TOPEX-A drift.

## 2.1.4. Uncertainty assessment

The uncertainties of the altimetry-based global mean sea level are computed using the method and information from Ablain et al. (2019) and updated by Guérou et al. (2023). Table 3 summarises the sources of uncertainties for the global mean sea level and their estimates. For the uncertainty of the radiometer WTC, unlike in Guérou et al. (2023), the uncertainty is not increased over Jason-3 period as the Jason-3 WTC drift is corrected with the correction provided by Brown et al. (2023). The Glacial Isostatic Adjustment (GIA) contribution to the global mean sea level uncertainty is not applicable to the component not corrected for the GIA effect as described in this section, but this uncertainty contribution may be considered while no other estimate is available for the GIA component (section 2.9). Using the values in Table 3, the covariance matrix of the global mean sea level is computed following the method from Ablain et al. (2019).

*Table 3: Sources of uncertainties of the global mean sea level and their estimates, adapted from Guérou et al. (2023). Values in bold font have been updated since the estimates published by Guérou et al. (2023). In gray, the GIA contribution to sea level uncertainty is not applicable to the*

*component not corrected for the GIA effect as described in this section, but this uncertainty contribution may be considered for any separate GIA component.*

Source of uncertainty		Temporal structure of the uncertainty	Standard uncertainty $u$
Short-time correlated errors due to precise orbit determination (POD), altimeter parameters, geophysical corrections		Correlated effects with correlation duration of 2 months	$u = 1.6$ mm for TP period $u = 1.2$ mm for J1 period $u = 1.1$ mm for J2 period $u = 1.0$ mm for J3 period $u = 1.3$ mm for S6MF period
		Correlated effects with correlation duration of 1 year	$u = 1.2$ mm for TP period $u = 1.1$ mm for J1 period $u = 1.1$ mm for J2 period $u = 1.0$ mm for J3 period $u = 1.2$ mm for S6MF period
Radiometer WTC stability		Correlated errors with correlation duration of 5 years	$u = 1.1$ mm
POD stability	Gravity fields	Correlated errors with correlation duration of 10 years	$u = 1.12$ mm for TP $u = 0.5$ mm for J1/J2/J3
	International Terrestrial Reference Frame (ITRF)	Linear time-correlated effect (also called "Drift")	$u = 0.1$ mm/yr
Inter-mission offsets		Offset	$u = 2.0$ mm for TPA/TPB $u = 0.6$ mm for TP/J1 $u = 0.2$ mm for J1/J2 $u = 0.2$ mm for J2/J3 $u = 0.6$ mm for J3/S6MF
Global Isostatic Adjustment (GIA) correction		Linear time-correlated effect (also called "Drift")	$u = 0.05$ mm/yr
Altimeter parameters stability		Linear time-correlated effect (also called "Drift")	$u = 0.7$ mm/yr for TPA $u = 0.1$ mm/yr for TPB

The uncertainties linked to the gridded sea level anomaly data are described by Prandi et al. (2021). As for the global mean uncertainty budget, the GIA contribution to sea level uncertainty is not applicable to the component not corrected for the GIA effect as described in this section, but this uncertainty contribution may be considered while no other estimate is available for the GIA component (section 2.9). Table 4 summarises the sources of uncertainties for the local sea level change. Within each cell of  $1^\circ \times 1^\circ$ , the covariance matrix of the local sea level change can be computed using the information from Table 4.

*Table 4: Sources of uncertainties of the sea level change and their estimates, from Prandi et al. (2021). Location dependent standard uncertainties are provided in the Prandi et al. (2020) dataset. In gray, the GIA contribution to sea level uncertainty is not applicable to the component not corrected for the GIA effect as described in this section, but this uncertainty contribution may be considered for any separate GIA component.*

Source of uncertainty	Type of error	Standard uncertainty u
Geophysical corrections and orbit determination	Correlated errors with correlation duration of 1 year	Location dependent, provided in Prandi et al. (2020)
Radiometer WTC	Correlated errors with correlation duration of 10 years	Location dependent, provided in Prandi et al. (2020)
Orbit determination	Drift	u = 0.33 mm/yr
GIA correction	Drift	Location dependent, provided in Prandi et al. (2020)
Inter-mission offsets	Offset	u = 10 mm for TPA/TPB and TPB/J1 u = 6 mm for J1/J2 and J2/J3

### 2.1.5. Known limitations

The vDT2021 version of C3S sea level anomaly data does not use the latest release of altimetry along-track data (vDT2024). For instance, the data from the latest reprocessing of TOPEX observations are not included yet.

Spatial correlations are not taken into account in the local sea level change uncertainties.

## 2.2. Steric sea level

### 2.2.1. Review of scientific background

The main mechanisms leading to the observed increase in global mean sea level rise are: (1) continental freshwater gained by the oceans from land ice melt (Greenland and Antarctica ice sheets and mountain glaciers), and (2) volume (density) change due to thermal expansion as the oceans warm (WCRP Global Sea Level Budget Group, 2018). Salinity changes due to land ice melt, river runoff, and changes in evaporation/precipitation increases have only second-order effects on global mean sea level (Gregory et al., 2019). In practice, however, salinity changes in density should also be considered when data are available because observations are not strictly global (Chambers et al., 2017). The combined effect of ocean temperature and salinity is known as

steric sea level, with the thermosteric sea level referred to as thermal contribution and halosteric sea level referred to as salinity contribution.

### 2.2.2. Selection of used data

Gridded temperature and salinity data are obtained from LOPS laboratory (ISAS20, Kolodziejczyk et al., 2023) and from the Met Office (EN4, Good et al., 2013). The ISAS20 dataset uses the temperature and salinity Argo floats only and is interpolated on 187 standard depth levels between 0-5500 m depth and 0.5°x0.5° global horizontal grid. ISAS20 gridded fields are available over 2002-2020. However, data over 2005-2020 are considered as Argo distribution is near global since 2005 (from 60°S to 60°N). EN4 dataset combines Argo floats with in expendable bathythermograph -XBT-, Conductivity-Temperature-Depth - CTD- and mooring data. EN4 temperature and salinity fields are interpolated on 42 standard levels between the surface and 5500m depth on a regular 1° global horizontal grid. We will consider the EN4 data over 1993-2022 corresponding to the satellite altimetry period. For both datasets, we will provide steric sea level time series down to 2000m depth.

### 2.2.3. Algorithms

Steric sea-level anomalies are estimated (Eq.1) by integrating, from the surface to 2000 m (that corresponds to the maximum depth of the Argo floats), the difference between a reference density as a function of depth and the density of seawater.

$$SSL(x, y, t) = - \frac{1}{\rho_0} \int_{2000}^0 (\rho(T(x, y, z, t), S(x, y, z), p) - \rho_{ref}(0, 35.16504, p)) dz \quad (Eq.1)$$

where  $SSL(x, y, t)$  is the steric sea-level anomaly at location  $x, y$  and time  $t$  (mm),  $\rho_0 = 1026 \text{ kg m}^{-3}$  is the surface seawater density,  $\rho(T(x, y, z, t), S(x, y, z), p)$  is the seawater density ( $\text{kg m}^{-3}$ ) with  $T(x, y, z, t)$  being the conservative temperature ( $^{\circ}\text{C}$ ),  $S(x, y, z)$  being the absolute salinity and  $p$  being the pressure (dbar).  $\rho_{ref}(0, 35.16504, p)$  is the reference seawater density ( $\text{kg m}^{-3}$ ) where temperature and salinity are constant ( $0^{\circ}\text{C}$  and  $35.16504 \text{ g/kg}$ , respectively) while the pressure varies. The parameters  $\rho$  and  $\rho_{ref}$  are computed with the Gibbs-SeaWater (GSW) toolbox.

The thermosteric sea-level is computed similarly as the steric sea-level (Eq.1) except that the salinity in  $\rho$  is kept constant. This constant salinity represents the time mean (invariant quantity) as a function of depth over 2005-2020 for ISAS20 and 1993-2022 for EN4 dataset.

The halosteric sea-level is computed similarly as the steric sea-level (Eq.1) except that the temperature in  $\rho$  is kept constant. This constant temperature represents the monthly mean climatology over 2005-2020 for ISAS20 and 1993-2022 for EN4 dataset.

### 2.2.4. Uncertainty assessment

Uncertainty assessment will be provided comparing two approaches. First, as done operationally along with ISAS and climate indices, the analysis error provided by the OI system on T and S will be propagated in the global Sea Level estimates, using vertical and horizontal correlation scale

estimated from the ISAS T/S fields (using the 20 years) and using the horizontal correlation scale provided in ISAS (~300 km) respectively. This will be performed in both real ISAS and synthetic ISAS. Second, this propagated uncertainty will be compared with the error derived from the RMSD between model truth and the synthetic ISAS. The analysis error propagation approach and choice of correlation scale for the error estimate will be discussed.

### 2.2.5. Known limitations

Temperature and salinity Argo profiles allow us to estimate global mean steric sea level with unprecedented accuracy at global scale since 2005. However, core Argo float coverage is not global and therefore presents some limitations. First, core Argo has been designed to assess ocean temperature and salinity within a spatial resolution of 3°. Thus, this observing system does not allow for eddy variability investigations that may leave imprints on regional steric sea level change. Second, core Argo distribution is not global. The current coverage is restricted to 60° latitudes and to the upper 2000 m of the oceans. More, marginal and semi enclosed seas have not been perfectly sampled since 2005. Therefore, this non global data distribution remains a limitation when assessing global mean steric sea level change. Fortunately, with the new Argo program known as One Argo, future priorities have been set to sample the polar regions, the deep ocean, and the marginal/semi-enclosed seas. These limitations have been identified and will be overcome with the ongoing expansion of Argo distributions.

## 2.3. Ocean mass from space gravimetry

### 2.3.1. Review of scientific background

The GRACE (2002-2017, Tapley et al., 2019) and GRACE-FO (launched 2018, Landerer et al., 2020) satellite gravity missions allow to observe temporal changes of Earth's gravitational field. They are provided as Level-2 (L2) global gravity field models in a spherical harmonic (SH) representation, typically at a temporal resolution of 1 month. The temporal gravity variations are caused by mass redistributions within the solid Earth (mainly GIA and tectonics) and at the Earth's surface (water, ice, atmosphere). If the gravity effects of solid-Earth processes are known and subtracted, the remaining temporal gravity field variations can be converted into temporal variations of the surface mass distribution (in units of mass per surface area). Integration over predefined regions (such as the global ocean) leads to temporal variations of surface mass in this region.

We derive surface mass changes from GRACE L2 SH solutions. This gives us full access to, and control of, methodological choices and uncertainty characterisation. As an alternative (used as backup and validation), Mascon solutions directly based on the analysis of L1 data (most importantly the inter-satellite ranging data) provide ready-made mass change estimates (Loomis et al., 2019; Save et al., 2016; Wiese et al., 2016).

### 2.3.2. Selection of used data

We use the ITSG2018 series of GRACE and GRACE-FO SH solutions (Kvas et al., 2019) expanded up to SH degree 96. This choice is based on previous assessments of a number of alternative L2 solutions series which have indicated that ITSG2018, together with, and slightly superior to, CSR RL06 have the lowest noise level together with the best signal retaining (Ditmar, 2022; Meyer et al., 2024). Another strong argument for ITSG2018 is the free availability of the formal error covariance matrices of the monthly solutions, which is instrumental for our L2-based mass change solution. The COST-G RL02 solutions (Meyer, 2020; Meyer et al., 2024) may be an alternative for their noise level that is still slightly lower than that of ITSG2018. However, they are not equipped with error covariance matrices.

We added degree-1 coefficients derived by combining the monthly solutions and assumptions on ocean mass redistribution (Bergmann-Wolf et al., 2014; Sun et al., 2016; Swenson et al., 2008). These degree-1 series are similar to those provided in TN-13 by the GRACE/GRACE-FO Science Data System (SDS), but are derived in-house consistent with the utilized ITSG2018 gravity field solutions and with the applied GIA correction. We replaced C20 coefficients with estimates based on satellite laser ranging provided in TN-14 (Loomis et al., 2019). We replaced C30 coefficients by TN-14 values for the time period starting from October 2016 in response to the GRACE and GRACE-FO accelerometer instrument issues (Loomis et al., 2019).

### 2.3.3. Algorithms

We derive monthly global grids of surface mass distribution anomalies, expressed as areal density in units of  $\text{kg/m}^2$ , from Level-2 monthly SH gravity field solutions. Mass changes of a certain area (such as the global ocean or the Antarctic Ice Sheet) are obtained by summing up the mass anomalies (areal density multiplied by grid cell area) from the grid cells belonging to this area. The methodology applied can be described from two perspectives related to two schools of thought and, in this way, reconciles these two perspectives (Döhne et al., 2023).

One perspective is the regional integration of areal density anomalies synthesized from the L2 gravity field solutions. Such a regional integration requires the definition of an integration kernel (or sensitivity kernel). The regional integration, and hence the sensitivity kernel, can be expressed either in the SH domain or in the spatial domain. Leakage effects and GRACE L2 error effects depend on this sensitivity kernel. We define sensitivity kernels that minimize, in a least-squares sense, the sum of leakage effects and GRACE L2 error effects. This method, called tailored sensitivity kernels, is described in detail by Groh and Horwath (2021). The formal optimisation requires stochastic information on the expected mass redistribution signal (signal variances and covariances) and on the GRACE L2 errors (L2 error variances and covariances). We derive one sensitivity kernel for each grid cell. The sensitivity kernels for compound regions arise as the sum of the sensitivity kernels associated to grid cells belonging to this region.

The alternative perspective is that of an inversion of mass changes from the L2 solutions. Mass changes are parametrized as a set of prescribed patterns. Scaling factors for each of these



patterns are estimated so that the gravity effect fits the L2 solution. Mascons (mass concentrations in a single grid cell) are the most generic definition of such patterns. Hence, this perspective can be termed as L2-based mascon solutions. Mascon solutions lend themselves to introducing a-priori information on the expected signal, such as geographically dependent signal variance and covariance. They also need to employ - implicitly or explicitly - a GRACE L2 error characterisation. Croteau et al. (2021) provide a recent exploration of the L2-based mascon methodology.

Döhne et al. (2023) showed that the two perspectives (regional integration with tailored sensitivity kernels and L2-based inversion, or L2-based mascons) are equivalent as long as they employ the same variance-covariance information on both the mass redistribution signal and the GRACE L2 errors. Our mass change solution is hence a further development based on the work at TU Dresden by Groh and Horwath (2021) and Döhne et al. (2023) and the L2-based mascon methodology as realized by, e.g. Croteau et al., 2021. Here we summarize the specific methodological choices made for the SLBC\_cci+ L2-based mass change product.

For the mascon inversion, mascons are defined at an equal-area (approximately 120 km x 120km) grid with latitude increments of 1.1° and latitude-dependent longitude increments. Each grid cell is assigned to one of three domains: ice sheet, land (other than ice sheet), or ocean. When assigning the domains, we pay particular attention to small islands known to carry considerable ice mass change (e.g. Franz Josef Land in the Arctic, or Kerguelen Island and South Georgia Island in the sub-Antarctic) to mitigate misassignment of their mass changes to the ocean domain. Mascons containing such islands are assigned to the land domain even if the island covers just a small fraction of the mascon area outside its geometric center.

To obey the standard grid format used as the interface for SLBC\_cci+, the mascon solutions are subsequently interpolated to 1° equal-angle grids. The interpolation is designed to ensure mass conservation within each of the three domains.

As a novel feature of our method, each mascon is not just a mass concentration in the center of its grid cell, but it is amended by a global pattern of ocean mass change that corresponds to the gravitationally consistent sea-level fingerprint of this mass concentration. This has two advantages. First, each mascon represents a globally mass-conserving pattern. Second, when constraining oceanic mascons through a prescribed signal variance, this constraint does not apply to ocean mass redistribution related to sea-level fingerprints but only to ocean-dynamic mass redistribution that occurs on top of the 'passive' fingerprints.

As for the GRACE L2 error variance-covariance information we incorporate the formal error covariance matrix of the ITSG2018 solutions. We take the mean matrix over the months from 2003-01 to 2016-08 and use this same matrix for every month of our solution.

As for the signal variance information prescribed to the inversion we follow an iterative procedure similar to Croteau et al. (2021), driven by the variance of the GRACE mass change time series. In the first iteration, the prescribed signal variances are based on the observed variances of EWH time series simply synthesized from the GRACE L2 solutions applying a 275 km Gaussian filter.



This observed variance is used for land and ice-sheet mascons. In the ocean domain the median of the variance over all ocean positions is used uniformly for each ocean mascon. In each of the following iterations, the signal variances are based on the temporal variance of the previous iteration. Still, prescribed ocean mascon variances are set uniformly to the median of observed ocean mascon variances. To avoid divergence of the data-driven iteration to zero variance values, we keep the prescribed variances within empirical thresholds: For any land or ice-sheet mascon with an observed variance below the 31.7 % quantile of all observed land and ice-sheet variances, the prescribed variance is set to this 31.7 % quantile. Similarly, mascons with observed variances above the 99.5 % quantile of all ice-sheet mascons are prescribed the value of this 99.5% quantile.

As for the signal covariance, we prescribe spatial covariance between mascons of the same domain (land, ice-sheet, or ocean) but not between mascons of different domains. We assume a Gaussian autocorrelation with a 300 km one-sigma correlation length.

The gravity effect of GIA is corrected from the GRACE solutions prior to their analysis, and prior to deriving and adding the degree-one coefficients. In the current version (as by 2024-10-07), the GIA model output ICE-6G\_D (VM5a) by Peltier et al. (2018) is used. This will be replaced by the GIA model output generated within SLBC\_cci+ (see Section 2.9). The PSD (Section 3.3 therein) elaborates on the necessity and the implications of this GIA correction.

Prior to the analysis of the monthly solutions, the AOD (atmospheric and oceanic de-aliasing model) applied during GRACE L2 product generation was re-added. More specifically, the so-called GAD fields (representing ocean-bottom pressure anomalies due to atmosphere and ocean dynamics) were re-added, except for the global-ocean mean value of these GAD fields. This strategy follows the recommendations by Uebbing et al. (2019).

Fig.2 and Fig.3 illustrate our global mass change product on the level of gridded mean linear trends and on the level of integrated mass changes over the global ocean, respectively.

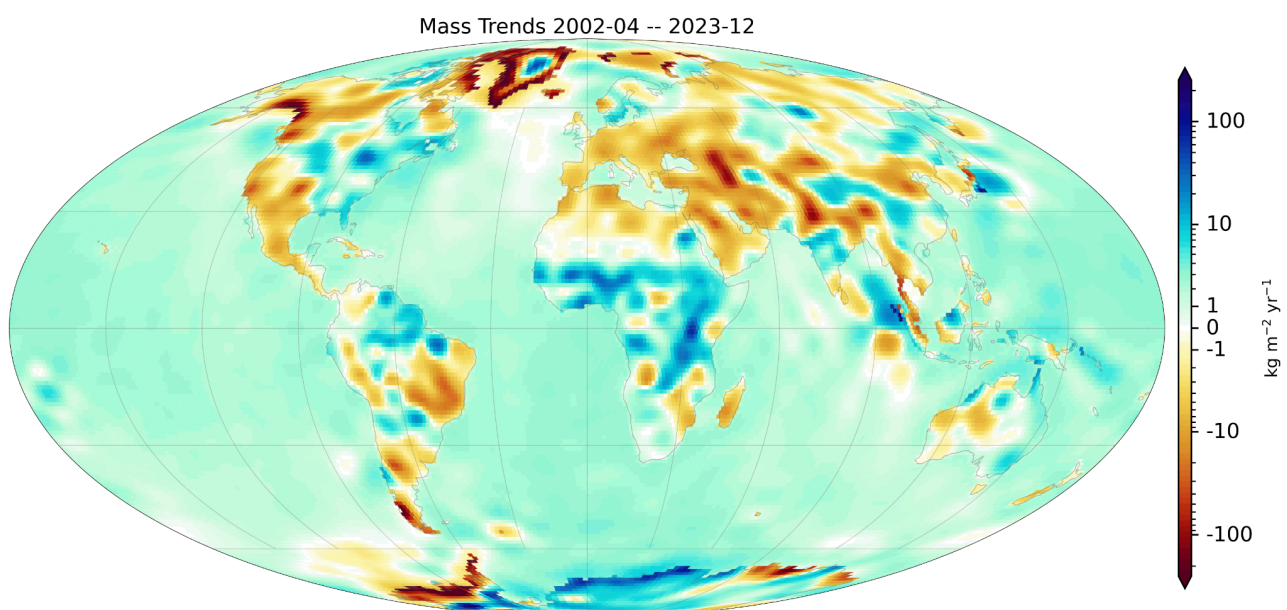


**Figure 2::** mean linear trend of surface mass distribution from satellite gravimetry over 2002-04 – 2023-12, from the Level-2 based mascon solution developed at TU Dresden.

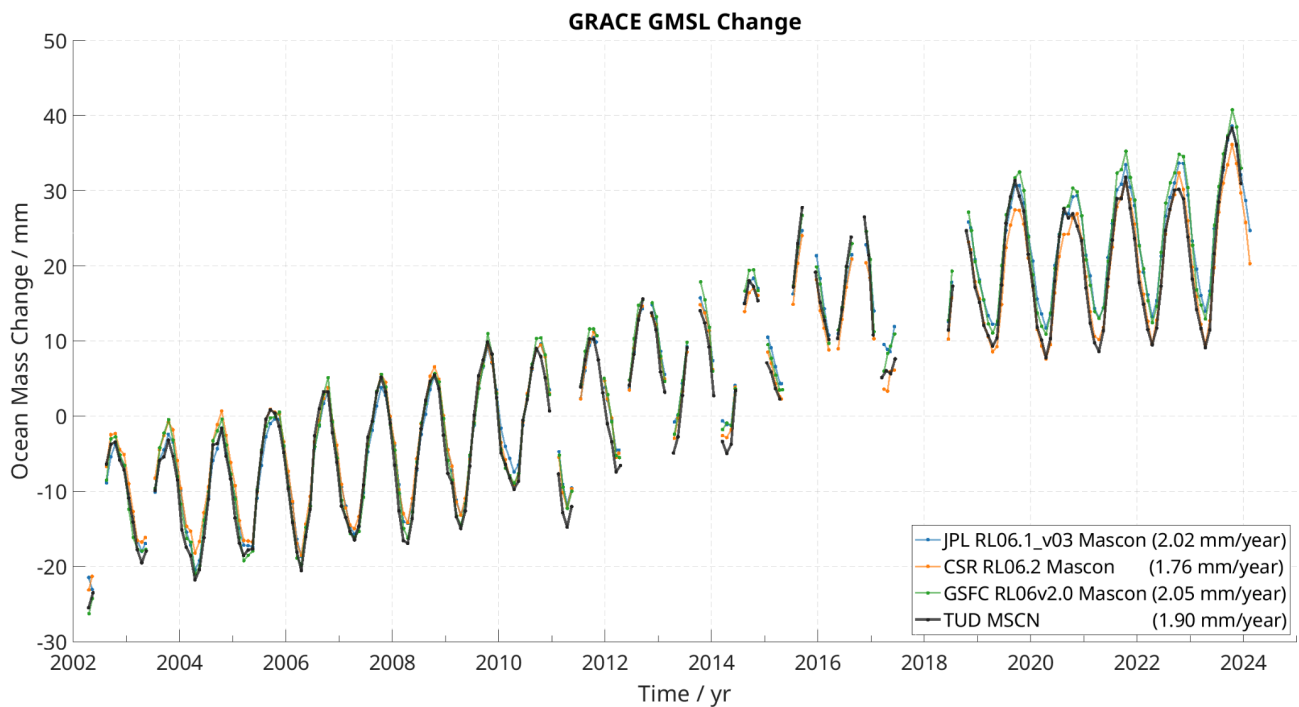


**Figure 3:** mass change of the global ocean, expressed in barystatic sea level, from the following satellite-gravity based solutions (see legend): L2-based mascon solution by TU Dresden (TUD MSCN, black) and L1-based mascon solutions by JPL (blue), CSR (orange), GSFC (green). Mean linear trends are quoted in the legend.

#### 2.3.4. Uncertainty assessment

We assess time-dependent error variances and covariances of our time series of regionally integrated mass changes, such as the global ocean mass change. This includes a separate assessment of errors from the following error sources:

- (a) uncorrelated noise propagated from the GRACE L2 solutions
- (b) errors propagated from the low-degree harmonics (degree-one, C20, C30)
- (c) leakage errors

- (d) errors of geophysical corrections, most importantly for GIA.

The methods to assess the individual error sources and to construct the related error covariance matrices are a refinement of the methods used by Groh and Horwath (2021), and we specify them in the following for error sources (a)-(d).

- (a) Following Groh and Horwath (2021) we assess the uncorrelated-noise component of the mass time series by the RMS of a high-pass filtered time series, scaled with a factor that compensates for the attenuation of the RMS of white noise by the high-pass filtering.
- (b) Following Groh and Horwath (2021) we use ensembles of alternative low-degree harmonics time series and take the spread of the ensembles as an indication of their uncertainty. Particularly, we use the spread of linear trends of the ensemble members to assess the uncertainty propagated to the linear trend of the mass change time series.
- (c) We assess leakage errors by simulations, similarly to Groh and Horwath (2021), but with an updated and extended set of synthetic models. The simulations use synthetic signals of terrestrial water storage changes, glacier mass changes, ice-sheet mass changes, and ocean dynamics changes. The synthetic signals are converted to their gravity field effect in the SH domain. After SH truncation to the maximum SH degree of the GRACE L2 solutions, they are then processed in the same way as the GRACE L2 solutions are processed. The difference between the resulting simulated mass change solutions and the original synthetic mass change models represent the simulated leakage effects. We consider the leakage effect as an autocorrelated stochastic process, and we consider the simulated leakage effects as a representation of this process. Our aim is to characterize this autocorrelated 'noise' by an analytical spectral model adjusted to the simulated leakage error time series. As the simplest, and most relevant, component of auto-correlated noise we assess its temporally linear component from the linear components of the simulated leakage error time series.
- (d) We consider GIA, and hence GIA model errors, as strictly linear in time over the 23 years of GRACE/GRACE-FO. Following Horwath et al. (2022) we assess the uncertainty of the GIA corrections from the spread among an ensemble of alternative GIA corrections.

Error covariance matrices of each individual error source are summed up to the full error covariance matrix of the mass change time series. Fig.4 illustrates the covariance matrix for global ocean mass anomalies.

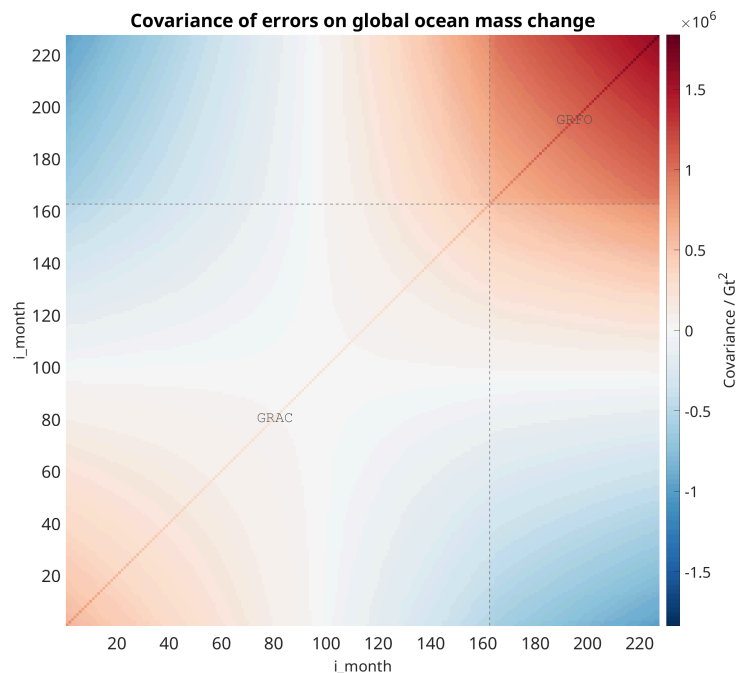


*Figure 4: Temporal error covariance matrix of the time series of global ocean mass anomalies corresponding to the TU Dresden L2-based mascon solution. The axis shows sequential numbers of the monthly solutions, irrespective of temporal gaps (most notably the GRACE – GRACE-FO gap between No. 162 and 163).*

Note that the characterisation of temporally correlated errors of mass anomalies depends on the reference to which the anomalies refer. Here this reference is the mean mass distribution over the 11-year period 2005-01 - 2016-12.

### 2.3.5. Known limitations

The solutions are not corrected for gravity field effects of plate tectonics and earthquakes. Effects of megathrust earthquakes (such as 2004 Sumatra-Andaman, 2010 Chile, 2011 Tohoku-Oki) lead to misattribution of the resulting signal between prescribed land and ocean domain and additionally show up as steps in the local ocean mass time series, leading to significant artefacts in linear trends derived from these time series, which are among the most prominent features in global gridded ocean-mass trend maps.

The uncertainty of the GIA correction remains a large source of uncertainty for global ocean mass change estimates from GRACE. For example, a likely trace of errors in the GIA correction can be found in the Barents Sea around 77°N/45°E.

The definition of the different domains – land, ice sheets, ocean – is a compromise not only due to the necessary discretisation but also due to practicalities of avoiding leakage effects. As an example, the whole Greenland island (even though 20% of its area are unglaciated) is attributed to the ice sheet domain, consistent with the practice of previously published mascon solutions. Grid cells that contain just a small fraction of land may be attributed to land or ice-sheet, as exemplified

above for small islands. The definition of land, ice-sheet, and ocean masks is not consistent across different published mascon products, which complicates comparison on grid level. Comparisons on the level of regionally integrated mass changes (e.g. of Greenland Ice Sheet mass changes) should integrate each mascon product according to its proper region definition (e.g. its specific Greenland Ice Sheet mask).

## 2.4. Ocean mass from land and atmosphere components: Greenland Ice Sheet

### 2.4.1. Review of scientific background

Three major approaches exist for the assessment of present-day ice-sheet mass balance with a significant role of satellite Earth observations (Otosaka et al., 2023b). The altimetry method uses repeated observations of ice-sheet surface elevation by satellite altimetry to infer surface elevation changes and, subsequently, volume changes and ice mass changes. The conversion from volume to mass information, or assumptions, on the processes leading to volume change, including changes in the thickness and density structure of the firn layer. The gravimetric method uses temporal variations of Earth's gravity field as determined by the satellite gravimetry missions GRACE and GRACE-FO to infer the underlying changes of mass distribution, including ice-sheet mass changes with a spatial resolution on the order of 300 km. The separation of mass redistribution of the solid Earth by GIA is among the important error sources for the gravimetric method. The input-output method (IOM) separately assesses surface mass balance (SMB) as diagnosed by atmospheric modelling, and ice discharge by ice-flow across the grounding line as assessed from surface flow velocities from satellite remote sensing in conjunction with ice thickness information. Ice mass change per drainage basin is the difference between SMB (the 'input') and ice discharge ('output').

### 2.4.2. Selection of used data

SLBC\_cci+ mainly relies on established, published datasets on ice-sheet mass balance.

#### **IMBIE-2\_R2 aggregated assessment** (cf. DARD Table 18 and Table 22)

The latest assessment of the ESA/NASA Ice-sheet Mass Balance Intercomparison Exercise (IMBIE-2\_R2, Otosaka et al., 2023a) compiled a total of 27 contributed mass balance assessment for GIS (23 for the AIS), comprising assessments from each of the major approach (altimetry, gravimetry, IOM). This aggregated assessment was an instrumental source for the IPCC AR6 assessment of ice sheets' sea-level contribution. The time span covered is 1992-01 to 2020-12.

#### **CCI GMB products** (cf. DARD Table 19 and Table 23)

The gravimetric mass balance (GMB) products of the GIS\_cci+ and AIS\_cci+ projects are based on the analysis of GRACE and GRACE-FO L2 gravity field solutions. They have been validated

within these two CCI projects and were used in the sea-level budget analysis by Horwath et al. (2022). The time span covered is 2002-04 to 2024-02.

**Alternative data products** exist, in particular for the GIS, such as the PROMICE dataset (DARD Table 21) and the GIS\_cci / SLBC\_cci GIS mass balance from calibrated radar altimetry (DARD Table 20). These datasets could be implemented as well. As there is generally good agreement between alternative mass balance estimates of the GIS (cf. Ootosaka et al., 2023a) we may expect little sensitivity of the global and regional sea-level budget assessment within the SLBC\_cci+ project to the choice of the GIA dataset.

### 2.4.3. Algorithms

#### **IMBIE-2\_R2 aggregated assessment**

The computed time series of mass change estimates are aggregated as documented in detail by Ootosaka et al. (2023a). The aggregation is in two steps: first among assessments following the same of the three approaches, and second across the three approaches. Each aggregation applies a weighting accounting for assessed uncertainties. The published dataset (see DARD Table 18 and Table 22) comprises time series from 1992-01 to 2020-12 at a monthly resolution of mass balance and its uncertainty (Gt/yr) as well as cumulative mass balance (since 1992-01) and its uncertainty (Gt).

#### **CCI GMB products**

The products include a monthly gridded product and a monthly basin-integral mass change product. The underlying methodology (Döhne et al., 2023; Groh et al., 2021) is similar (a methodological predecessor) to the methodology described in Section 2.3.

The time series contains mass anomalies w.r.t. 2011-01-01 (according to the 2011-01-01 value of a functional fit to the period 2002-08 - 2016-08).

An ellipsoidal correction following Ditmar (2018) was recently added to the GMB products, which is not yet implemented in the SLBC\_cci+ ocean mass from space gravimetry product described in Section 2.3. Different GIA models are applied in the GIA correction for the two ice sheets: the model IJ05\_R2 (Ivins et al., 2013) for the AIS, and the weighted ensemble mean GIA solution by Caron et al. (2018) for Greenland.

### 2.4.4. Uncertainty assessment

#### **IMBIE-2\_R2 aggregated assessment**

Uncertainties from the contributed assessment are propagated through the aggregation procedure by the formalism detailed by Ootosaka et al. (2023a). Since the cumulative mass balance is w.r.t. the start of the time series in 1992-01, given uncertainties of the cumulative are also w.r.t. this starting time and consequently increase monotonically in time. Uncertainties of cumulative mass



anomalies w.r.t. a different reference time can be generated by cumulating the uncertainties of the mass balance rates w.r.t. the new reference time, adapting Eq. 7 of Otosaka et al. (2023a).

### CCI GMB products

Uncertainties of the monthly mass anomalies are modelled as the combined effect of uncertainties of the temporal linear trend,  $\sigma_{\text{trend}}^2$ , and a temporally uncorrelated noise,  $\sigma_{\text{noise}}^2$ . The uncertainties of linear trends are summed up in quadrature from uncertainties due to different error sources (b, c, d outlined in Section 2.3.4). The trend uncertainties are given separately (in the separate file AIS\_GMB\_trend.dat, GIS\_GMB\_trend.dat). In this way, it can be propagated to monthly uncertainties w.r.t. a reference time of the user's choice. The error variance at any epoch is then  $\sigma_{\text{total}}^2(t) = \sigma_{\text{noise}}^2 + \sigma_{\text{trend}}^2 (t - t_0)^2$ .

### 2.4.5. Known limitations

#### IMBIE-2\_R2 aggregated assessment

Some limitations are discussed by Otosaka et al. (2023a).

There is some ambiguity about the inclusion or exclusion of peripheral glaciers, which are typically excluded in altimetry and IOM assessments, but included, or poorly separated, in gravimetry assessments.

While the formal temporal resolution of the aggregated dataset is monthly, the effective temporal resolution of some of the input assessments (notably from altimetry) is coarser, so that the time series are unlikely to reflect the full month-to-month variability of mass balance.

There is no spatial resolution of the aggregated dataset other than subdividing the AIS into WAIS, EAIS and AP.

The methodology of aggregating mass balance uncertainties in time does not consider temporal correlations of the monthly mass balance uncertainties. This limits the ability to reflect systematic uncertainties such as the GIA-related uncertainty of gravimetric estimates or firn-density related uncertainties and spatial-sampling related uncertainties for altimetric estimates.

### CCI GMB products

Monthly temporal sampling is not complete, with an 11-month gap 2017-07 to 2018-05 and an additional number of single months missing.

While the methodology attempted to separate mass changes of the proper ice sheet from mass changes of peripheral glaciers, the limited sensitivity of GRACE and GRACE-FO to spatial scales smaller than 200 km (in polar regions), limits the fidelity of this separation, a problem that is commonly expressed as leakage effect.

## 2.5. Ocean mass from land and atmosphere components: Antarctic Ice Sheet

### 2.5.1. Review of scientific background

The scientific background is summarized above in Section 2.4.1

### 2.5.2. Selection of used data

The description of data selection for the AIS is included in Section 2.4.2 above.

### 2.5.3. Algorithms

The description of algorithms for the AIS is included in Section 2.4.3 above.

### 2.5.4. Uncertainty assessment

The description of the uncertainty assessment for the AIS is included in Section 2.4.4 above.

### 2.5.5. Known limitations

The discussion of limitations for the AIS datasets is included in Section 2.4.5 above.

## 2.6. Ocean mass from land and atmosphere components: Glaciers and ice caps

### 2.6.1. Review of scientific background

As with the ice sheet mass balance, several methodologies are available, and have been used, to determine GIC mass trends for different epochs dependent on the approach and data available. The methods used comprise i) statistical modelling constrained by in-situ observations and reanalysis (e.g. Marzeion et al., 2012, 2015), ii) gravimetric estimates during the GRACE period with limitations related to signal to noise ratio for smaller glaciated regions (e.g. Wouters et al., 2019), stereophotogrammetric DEM differencing primarily from ASTER imagery (e.g. Hugonnet et al., 2021) with limitations in the temporal fidelity of the data but high spatial resolution down to individual glacier scale and, most recently, reconstructions using CryoSat-2 which provides improved temporal resolution at quasi-annual scale with some information the amplitude of the seasonal cycle but at coarse spatial resolution and limited capability in areas of high relief such as High Mountains Asia (HMA), which possess the largest volume of GIC outside of the polar regions (Fig.5). None of the satellite datasets mentioned above extend back to 1992, with ASTER being the earliest starting in 2000. Furthermore, no approach is entirely satisfactory in capturing both the spatial and temporal resolution required here. The statistical modelling approach can reconstruct mass balance for any period that has reanalysis or adequate climate data as input but has substantial uncertainties for several GIC sectors especially those where marine terminating



glaciers (MTG) are pervasive (Bamber et al., 2018). In these sectors, largely located in the Arctic (Fig.5), mass loss can be dominated by calving which has a complex relationship to climate, unlike surface melt. Attempting to address these issues Bamber et al., 2018 derived a GIC reconstruction for the satellite era by combining GRACE and statistical modelling by calibrating the former with the latter. More recently, an improved and more extensive method, using a similar concept, has been developed by the WGMS group (Dussaillant et al., 2024). Here they take the high resolution ASTER DEMs differences from Hugonnet et al., 2021 and combine them with sparse, but (sub)annual resolution, in situ mass balance data to provide the temporal resolution at a regional scale. The approach is similar to a fingerprint method: the assumption is that the inter-annual variability is driven by regional climate and therefore has a regional fingerprint and the spatial pattern can then be scaled accordingly (Dussaillant et al., 2024).

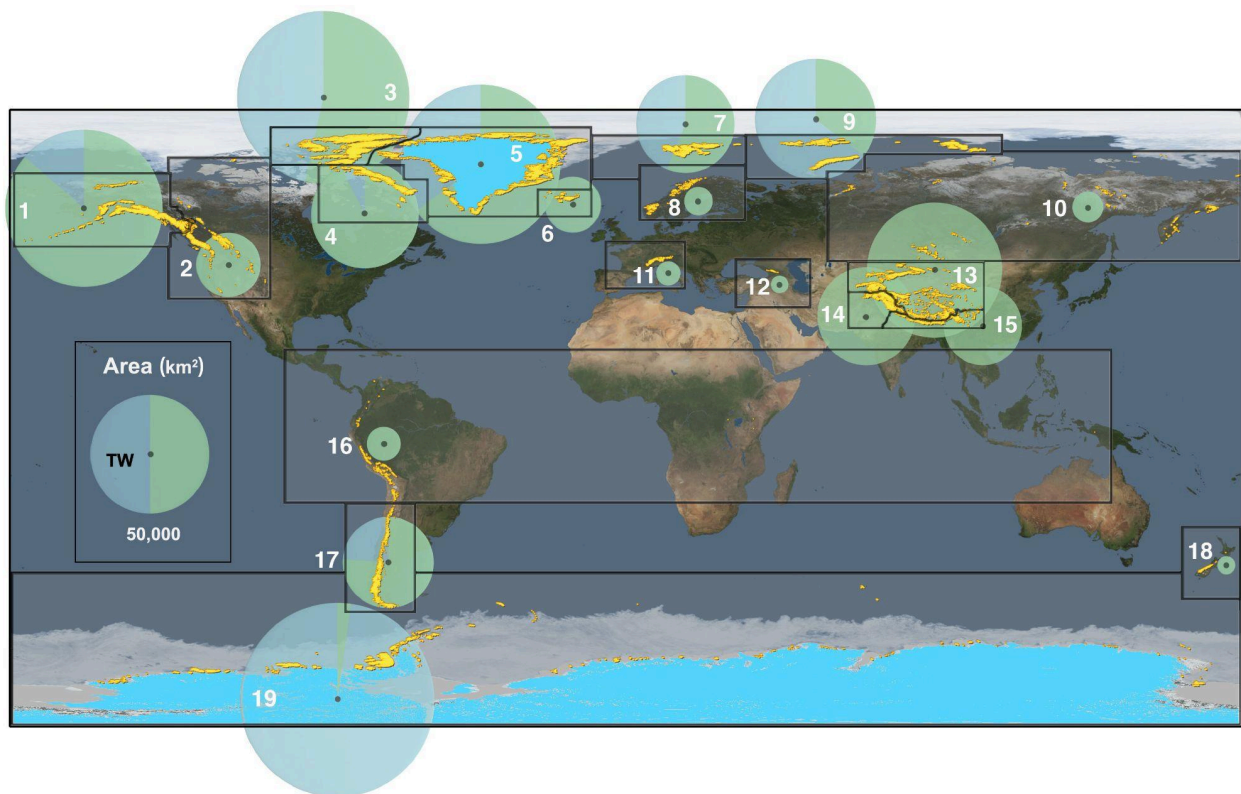


*Figure 5: Ice sheet (blue) and the 19 GIC sectors (yellow) that are part of the mass exchange estimates provided for land ice. The size of the circles represents the glaciated area and the percentage that is blue or green represents how much of the area is marine terminating or land terminating respectively.*

## 2.6.2. Selection of used data

As explained above, the choice of dataset to use was driven by the need for seasonally and locally resolved mass balances for GIC sectors extending back to 1992. The only viable and reliable dataset that satisfies all these conditions is the hybrid satellite/in-situ product developed by WGMS

(Dussaillant et al., 2024). This product has been provided to the Copernicus Climate Change Service as a curated dataset. It is available at 0.5 degrees spatial resolution for each of the 19 GIC sectors defined by WGMS at annual resolution from 1976-2023 and is described in detail in Dussaillant et al., 2024 and in Fig.6.

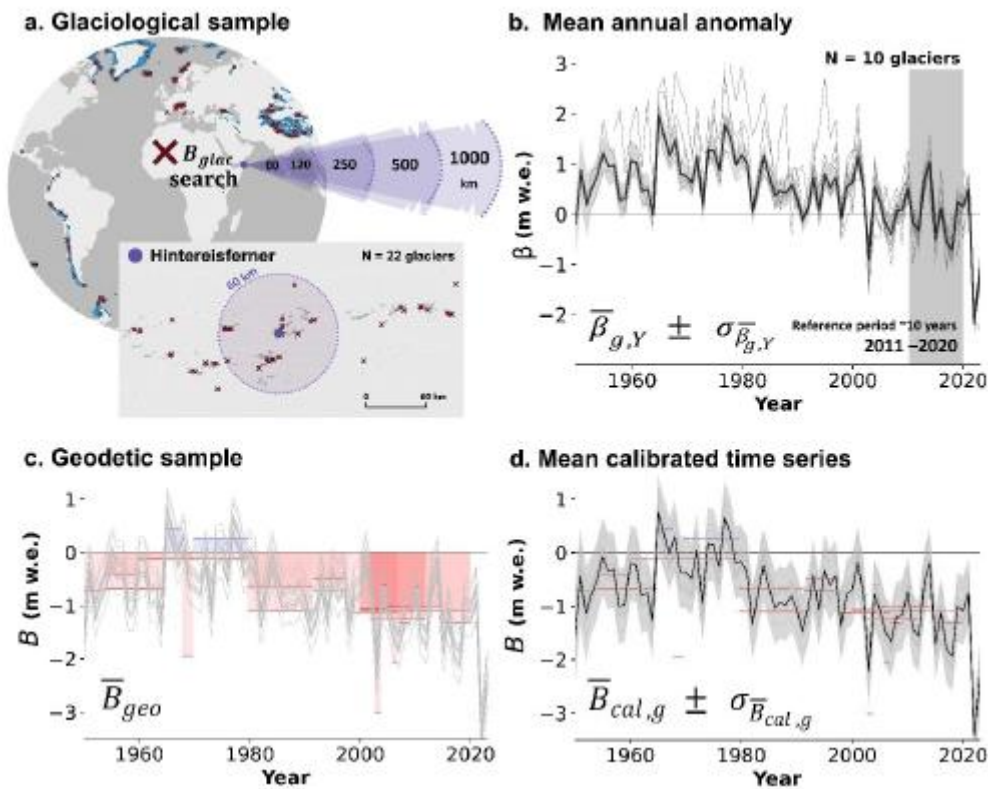


Figure 6: Illustration of the methodology (From (Dussaillant et al., 2024); a) illustrates the search area around the glacier where in situ observations exist that overlap with the ASTER data, b) shows the time series for the 10 glaciers in the search area, c) shows the geodetic data for the glacier used to calibrate the in-situ data and d) is the new calibrated time series for the glacier with uncertainties.

Here, we use a modified version of this dataset that includes an idealised seasonal cycle. Detailed in Fig.7.

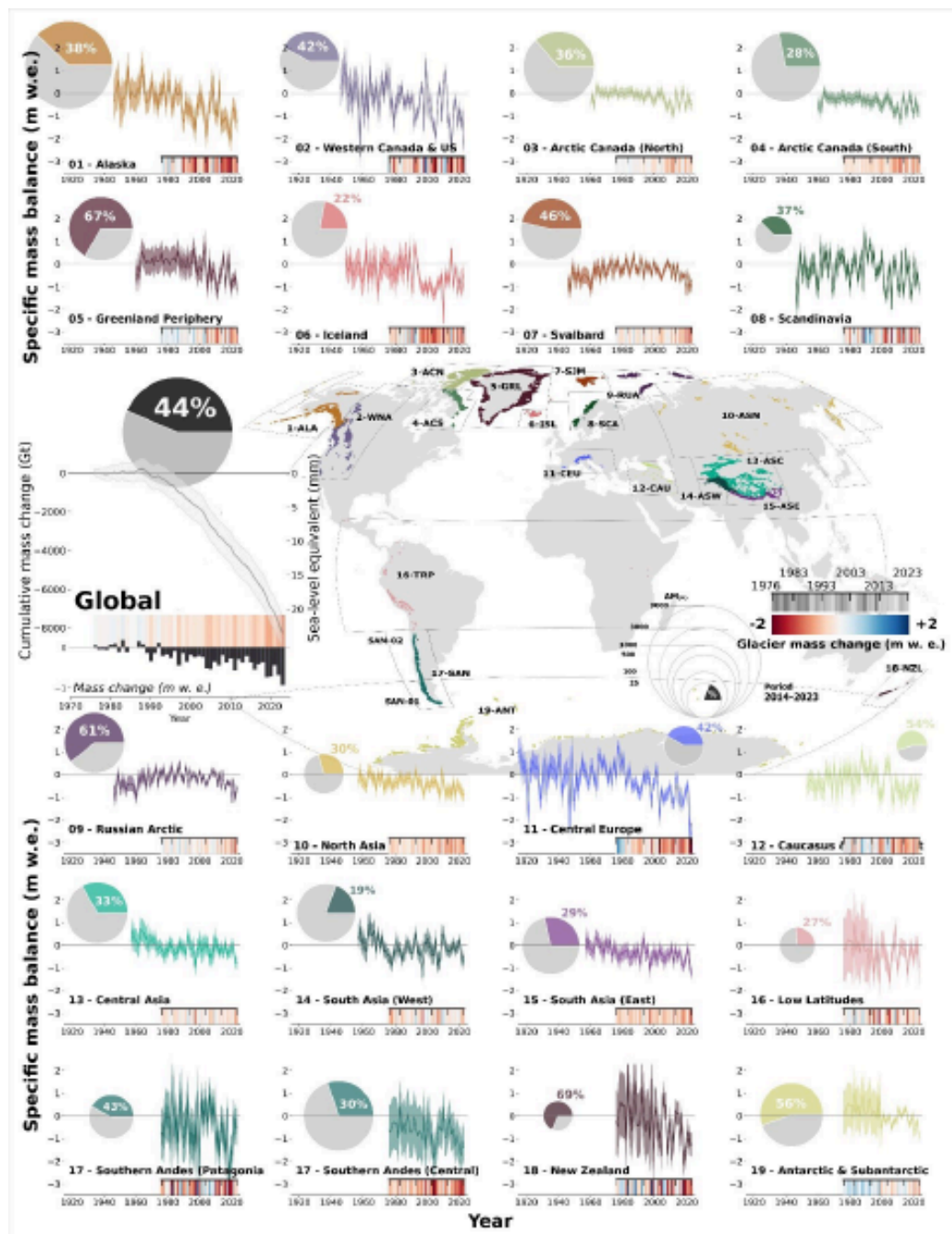


Figure 7: The mass balance time series at annual time resolution for all 19 sectors, alongside the 2-sigma uncertainties. Calibrated mass balance times series for all 19 GIC sectors. The area of the pie charts represents the mass lost since 1976 and the coloured region the mass loss from 2014-2023.

### 2.6.3. Algorithms

The algorithm used to derive the time series is explained in detail in (Dussaillant et al., 2024) except for one difference. Here, we required seasonal resolution for the mass trend as, for most sectors, there is a large seasonal cycle of winter growth and summer melt (except for tropical glaciers). The annual data were seasonally interpolated using the (Zemp and Welty, 2023) sine wave function, using the assumption that the hydrological year in the northern hemisphere runs from 1st October to 30th September and in the southern hemisphere from the 1st April to 31st March. The approach has been shown to capture well the seasonal cycle at roughly monthly time steps (Zemp and Welty, 2023).

### 2.6.4. Uncertainty assessment

A careful uncertainty assessment was undertaken using a leave one out cross validation approach (Dussaillant et al., 2024) and the two-sigma uncertainty for each 0.5 deg region and each time step is provided with the data. At a global scale the uncertainty in mass loss (depending on the exact time period) is about 11-12%. Over the five decades of the complete time series this equates to an uncertainty of +/-27 Gt/yr averaged across the 19 sectors (i.e. less than 0.1 mm SLE globally).

### 2.6.5. Known limitations

Some GIC sectors have few in-situ observations that can be used for temporal fidelity making those sectors less reliable at annual resolution but not influencing the long term (decadal) trend. On the other hand, there are few geodetic data prior to 2000 that can be used to “fingerprint” the spatial pattern of mass loss and to assess how stable in time it is. As a consequence, in general, data prior to 2000 has higher uncertainties than after this year.

## 2.7. Ocean mass from land and atmosphere components: Land water storage

### 2.7.1. Review of scientific background

The land water storage (LWS) variations contribute to sea level change through exchanges of water between land and oceans. The LWS variations encompass variations from various water reservoirs over land: snow, canopy, soil moisture, groundwater, lakes, reservoirs, wetland and rivers:

$$LWS = snow + canopy + soil\ moisture + groundwater + lakes + reservoirs + wetland + rivers \quad (Eq.2)$$

LWS variations are due both to natural variability (climate-driven contribution) and to anthropic activities (anthropogenic or human-induced contribution). The climate-driven contribution seasonal and inter-annual variations, without any strong long-term trend. Concerning the human-induced contribution, while it was negligible over the XXth century (i.e. over the 1900s), Cáceres et al.

(2020) shows that it has been increasingly important over the last decades, reaching a contribution of about 0.37 mm/yr over 2003-2016.

The total terrestrial water storage (TWS) variations defined as the water budget between precipitation, evapotranspiration and runoff includes the LWS and the land ice contribution:

$$TWS = precipitation - evapotranspiration - runoff = LWS + glaciers \quad (Eq.3)$$

In this section, we are interested in the LWS contribution, including the anthropogenic contribution and excluding the contribution of glaciers already addressed in section 2.6.

We provide here a non exhaustive view of available hydrological models for the LWS component, shown on Fig.8.

- The Water Global Assessment and Prognosis (WaterGAP) Hydrological Model (WGHM) version 22e (Müller Schmied et al., 2023) provides estimates of LWS using the fifth generation of the European Centre for Medium-range Weather Forecasts (ECMWF) atmospheric reanalysis (ERA5) and W5E5 datasets for the climate-forcing, with and without the anthropogenic contribution. The W5E5-based data are provided until the end of 2019 while the ERA5-based data are provided until the end of 2022.
- The ISBA-CTRIP (Interaction Soil-Biosphere-Atmosphere, Total Runoff Integrating Pathways from the Centre National de Recherches Météorologiques) hydrological model provides estimates of climate-driven LWS until the end of 2018 (Decharme et al., 2019).
- The GRACE-REC model is an estimate of the climate-driven TWS based on precipitation and calibrated against GRACE data (Humphrey and Gudmundsson, 2019) using three climate forcing models (ERA5, GSWP3 and MSWEP) and two GRACE datasets (from GSFC and JPL) until the end of 2014 when using GSWP3, until the end of 2016 when using MSWEP and until the end of 2019 when using ERA5. These estimates based on precipitations include the contribution of land ice.



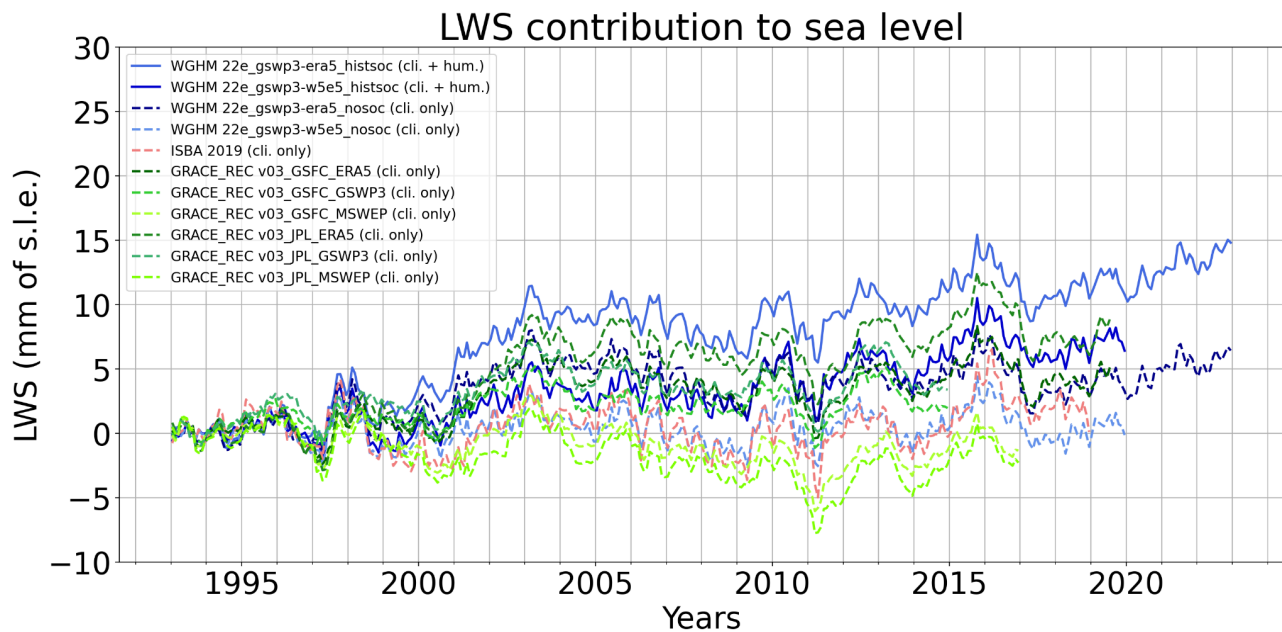


*Figure 8: Comparison of the estimate of land water storage variation contribution to sea level change from various hydrological models: four estimates of the WaterGAP Hydrological Model (WGHM) version 22e, the ISBA-CTRIP hydrological model and six estimates of the GRACE\_REC model. Plain lines indicate estimates including the human-induced contribution (“hum.”) while dotted lines indicate estimates taking into consideration only the climate-driven contribution (“cli.”). Only the GRACE-REC estimates include the land ice contribution.*

Note that ESA CCI datasets are available for the snow, soil moisture and lake contributions to LWS but estimates for other land water reservoirs are missing to estimate the full LWS component from CCI data. Hence, these are not used here.

## 2.7.2. Selection of used data

We use as a component the WGHM 22e estimate with anthropogenic contribution and using the ERA5 climate forcing as this time series is the only one provided until the end of 2022. Besides, this estimate does not include the contribution of land ice which is taken into account by the glacier component (see section 2.6).

Fig.9 shows the LWS time series used as a component for the sea level budget with its standard uncertainty. The full covariance matrix is estimated. The derivation of the component is described in section 2.7.3 and the uncertainty estimate is explained in section 2.7.4.

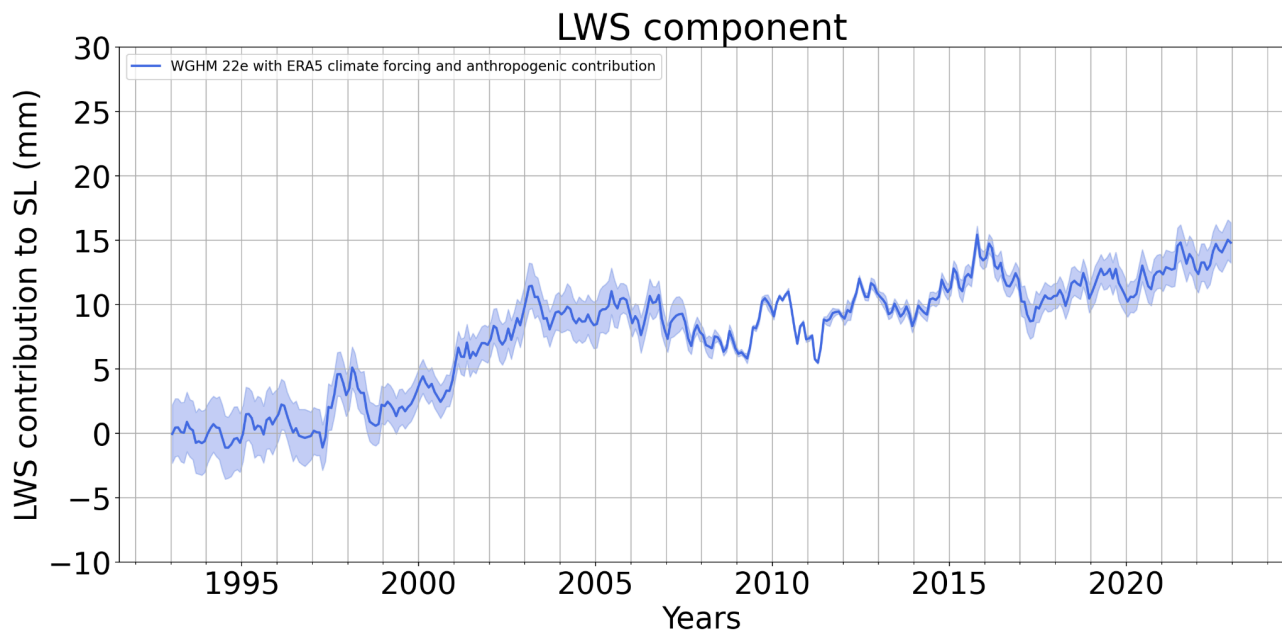


*Figure 9: Land water storage variations contribution to global mean sea level change, from the WaterGap Hydrological Model (WGHM) version 22e using ERA5 climate forcing and including the anthropogenic contribution.*

### 2.7.3. Algorithms

From gridded LWS data, we compute the global mean LWS variations over land areas excluding Greenland, Antarctica and glacier areas. The global mean LWS variation over land is then converted to contribution to sea level change using the total surface of oceans.

### 2.7.4. Uncertainty assessment

The uncertainty budget of the land water storage component includes two types of uncertainties:

- First, the uncertainty on the LWS trend, both for the climate-driven and anthropogenic contributions (Fig.11, green curve). We use the estimates obtained by Cáceres et al. (2020) over 1976-2002 (while the period does not perfectly coincide with our study period of 1993-2022, the time span is similar): -0.02 to 0.04 mm/yr for the climate-induced contribution and 0.14 to 0.25 mm/yr for the human-induced contribution. We use the range of these estimates as standard trend uncertainties, that is to say 0.06 mm/yr and 0.11 mm/yr for the climate-induced and human-induced contributions respectively.
- Second, we add white noise computed from the dispersion of the four WGHM solutions (ERA5 and W5E5 climate forcing and including or not the anthropogenic contribution, Fig.10a). Based on the difference of the ERA5 forced estimates, with and without anthropogenic contribution, the anthropogenic contribution is added to all time series that do not include the anthropogenic contribution (Fig.10b). The trend is removed from all time

series (Fig.10c) as the trend uncertainty is already taken into account as described above. The standard deviation of the four curves is used as uncertainty (Fig.11, blue curve). The GRACE-REC estimates are not used for the uncertainty assessment as they include the land ice contribution while we address this component in section 2.6.

The combination of the two trend uncertainties and of the white noise results in a full covariance matrix of the LWS component, following the same methodology as for altimetry (Ablain et al., 2019; Guérou et al., 2023). The resulting standard uncertainty of the LWS time series is the orange curve on Fig.11. The period of reference used for the computation of uncertainties is 2005-2015 included. In other words, the uncertainty relates to the variations of LWS with respect to the average of LWS over 2005-2015.

### 2.7.5. Known limitations

We have only one hydrological model providing estimates of LWS including the anthropogenic contribution and excluding the land ice contribution until the end of 2022.

Besides, the uncertainties associated with the LWS component are likely to be underestimated. While we rely on the work of Cáceres et al. (2020) for the trend uncertainties, we only add white noise based on a few time series, not taking into account any time correlations.



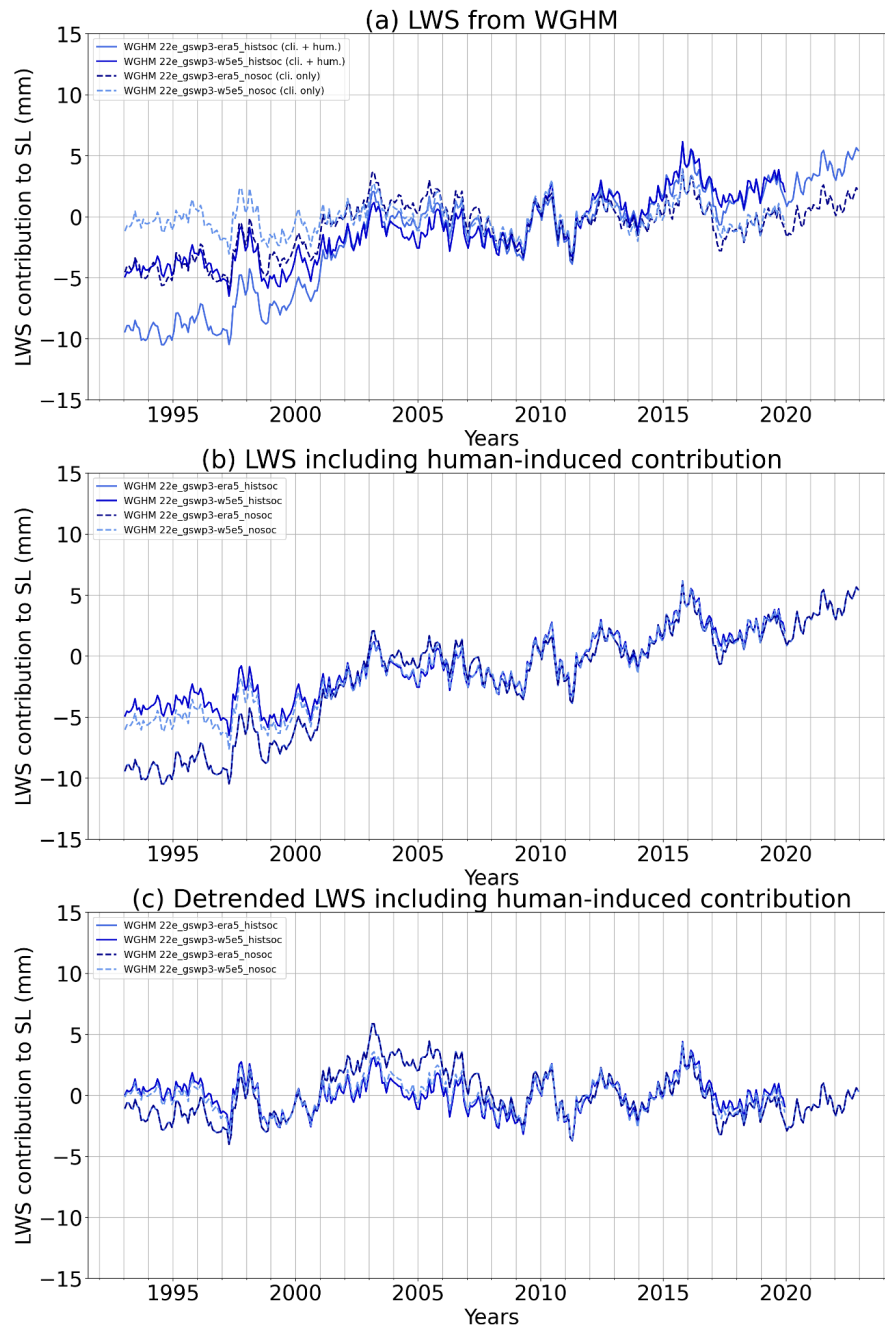


*Figure 10: Construction of ensemble of the estimate of the land water storage contribution uncertainty, using four WGHM 22e datasets. (a) WGHM 22e LWS contributions to global mean sea level with ERA5 and W5E5 climate forcing, with and without taking into account the anthropogenic contribution. (b) The anthropogenic contribution estimated from the differences between the two ERA5-forced timeseries is added to the timeseries without anthropogenic contribution. (c) Detrended time series.*

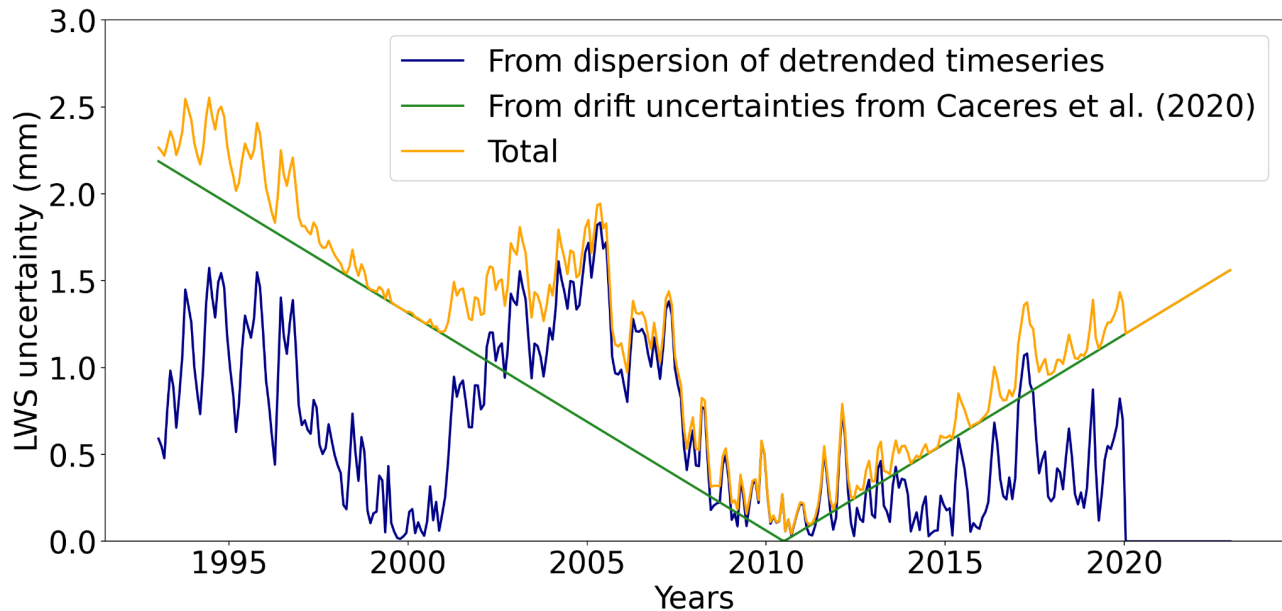


*Figure 11: Standard uncertainties of the land water storage contribution component. The blue curve results from the standard deviation of the ensemble of detrended estimates (see Fig.10c). The green curve accounts for the trend uncertainties for the climate-driven and human-induced contributions provided by Cáceres et al. (2020). The orange curve is the resulting combined standard uncertainty.*

## 2.8. Ocean mass from land and atmosphere components: Atmosphere water vapour

### 2.8.1. Review of scientific background

Global mean ocean mass changes are due to land water variations over land (both liquid water and ice) and to water vapour content change in the atmosphere. The atmospheric water vapour contribution to sea level change involves the whole atmosphere, both over land and over oceans. The water vapour content in the atmosphere is commonly referred to as total column water vapour (TCWV) or precipitable water. This contribution is very low, estimated to about -0.04 mm/yr over 1993-2015 by Dieng et al. (2017) and to about -0.08 mm/yr over 2005-2018 by Barnoud et al. (2023) based on ERA5 data.

### 2.8.2. Selection of used data

We use the ERA5 monthly  $1/4^{\circ} \times 1/4^{\circ}$  TCWV data that are available until present.

Fig.12 shows the atmosphere water vapour contribution to sea level change based on ERA5 and its standard uncertainty. The derivation of the component is described in section 2.8.3 and the uncertainty estimate is explained in section 2.8.4.

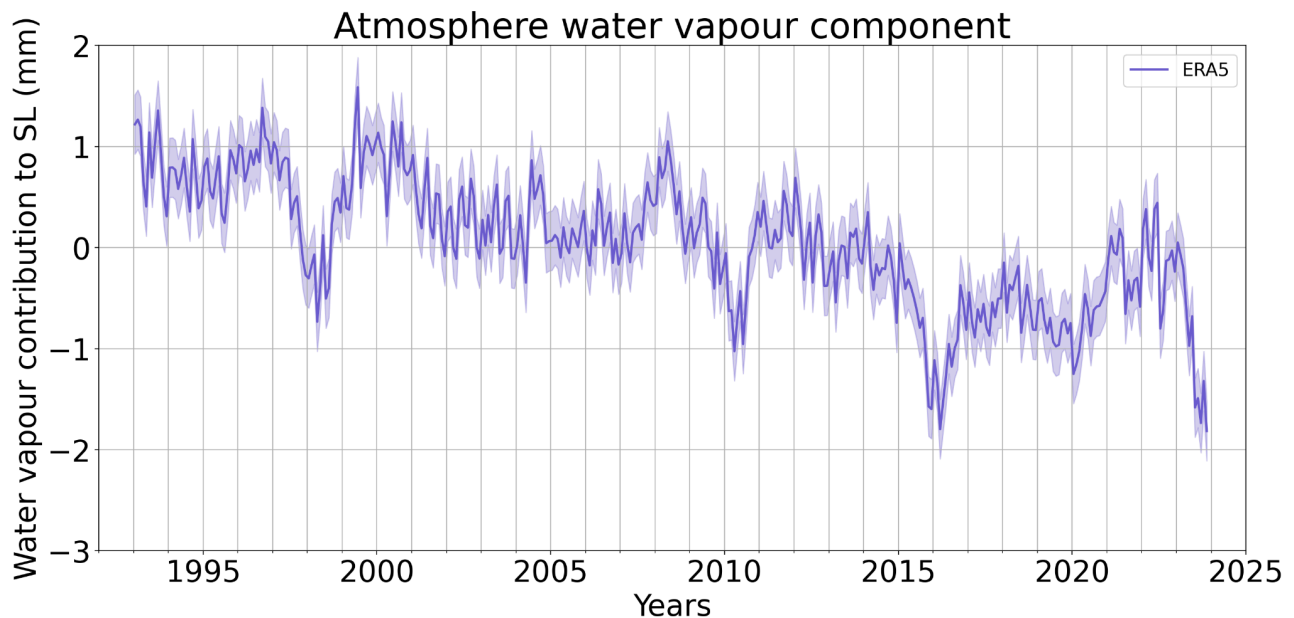


*Figure 12: Atmosphere water vapour content change contribution to global mean sea level change, computed from ERA5 total column water vapour data.*

### 2.8.3. Algorithms

The TCWV data are summed over the whole globe and converted to contribution to sea level change using the total surface of oceans.

### 2.8.4. Uncertainty assessment

In order to obtain an uncertainty estimate on the atmosphere water vapour component, we compare the ERA5 estimates with the sum of estimates from the ESA CCI over land and from the Hambourg Ocean-Atmosphere Fluxes and Parameters from Satellite (HOAPS) data over oceans (Fig.13a). The availability of this combined dataset is limited to 2002-2017 due to the time range of the CCI dataset. Over the common period between ERA5 and CCI+HOAPS estimates, the standard deviation of the difference is computed and used as standard uncertainty of a white noise uncertainty (Fig.13b).

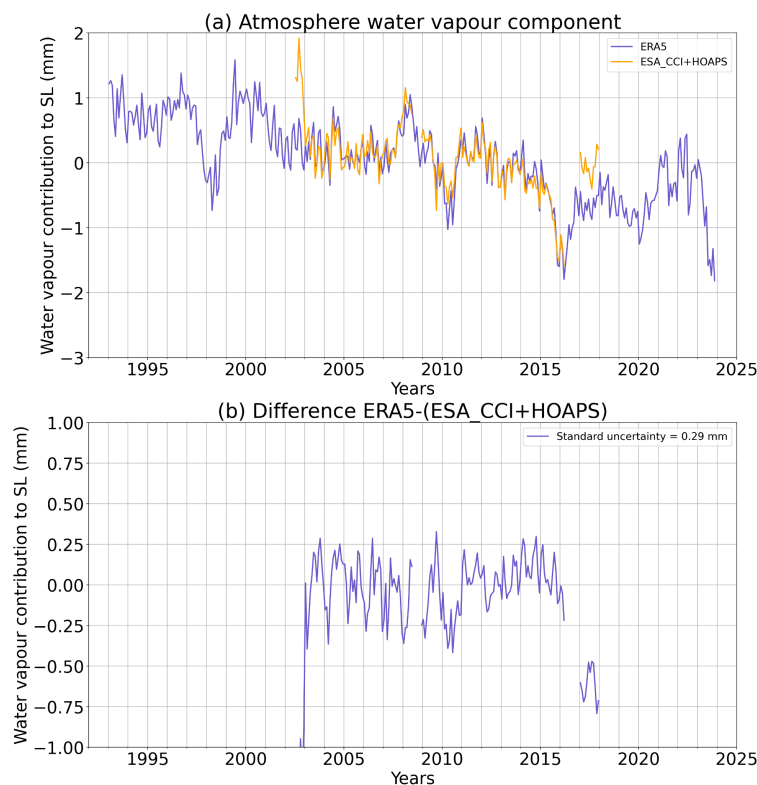


*Figure 13: Comparison of the atmosphere water vapour contribution estimated from ERA5 and from the sum of the ESA CCI water vapour data over land and of the HOAPS water vapour data over the oceans. (a) Time series. (b) Time series difference.*

### 2.8.5. Known limitations

No temporal correlations are taken into account in the uncertainty estimates associated with the atmosphere water vapour component.

## 2.9. Fingerprints and GIA

### 2.9.1. Review of scientific background

The fingerprints (Fig.14) and GIA (Fig.15) signals are the results of deformational, gravitational and rotational effects on sea level, driven by surface load redistributions of short (decades to centuries) and long (millennia) time scales, respectively. Both are solutions of the “Sea level Equation” (SLE) introduced in (Farrell and Clark, 1976) and later revised by a number of authors to include new physical features (earth’s rotational variations, migration of the shorelines, transition from grounded to floating ice). Solving the SLE gives access to various physical quantities, namely relative sea level change (S), absolute sea level change (N), vertical displacements of the crust (U), and geoid height change (G), which fully characterise the Earth’s response. For a review and references, see (Spada and Melini, 2019).

### 2.9.1. Selection of used data

For the elastic fingerprints, the input data selected are the accumulated effect of ice sheets and terrestrial water storage as well as individual components associated with major cryospheric sources (GrIS, AIS and small glaciers) and land water storage. These sources have been discretized according to the algorithm requirements. The Earth's elastic structure, necessary to evaluate the Green's functions, corresponds to the seismic model STW105 of (Kustowski et al., 2008). For the GIA component, in order to describe the Earth's topography, we have used the ETOPO1 elevation model integrated with the Bedmap2 relief south of 60°S latitude. The evolution of the ice sheets corresponds to the global ICE-6G\_C model at 500 years increments and the Earth rheological profile is the VM5a viscosity model (Argus et al., 2014; Peltier et al., 2015).

### 2.9.2. Algorithms

Established and benchmarked methods have been employed in order to solve the SLE. The elastic fingerprints and the GIA have been obtained by solving the Sea level Equation according to an iterative pseudo-spectral algorithm to harmonic degree LMAX=512 on an icosahedron-based equal area grid, using the open source code SELEN4. The algorithm is explained in detail in the work of (Spada and Melini, 2019), and briefly in the PSD.

### 2.9.3. Uncertainty assessment

The uncertainty on the computed fingerprints have two sources: *i)* the finite discretization of the Sea Level Equation, *ii)* the assumption of a specific 1D structure of the elastic Earth model (seismic model STW105, in this case). We have verified that these do not exceed the +/- 5% level on the computed fingerprints for S, U, N, and G. The GIA uncertainties have been evaluated as ensemble standard deviations (1-sigma) over the 20 variations of the VM5a rheological profile considered in (Roy and Peltier, 2015).

### 2.9.4. Known limitations

For the elastic fingerprints, one limitation is the assumption of a spherically symmetric Earth. For GIA, the same, and in addition to that, the assumption of incompressibility of the Earth's mantle and lithosphere.

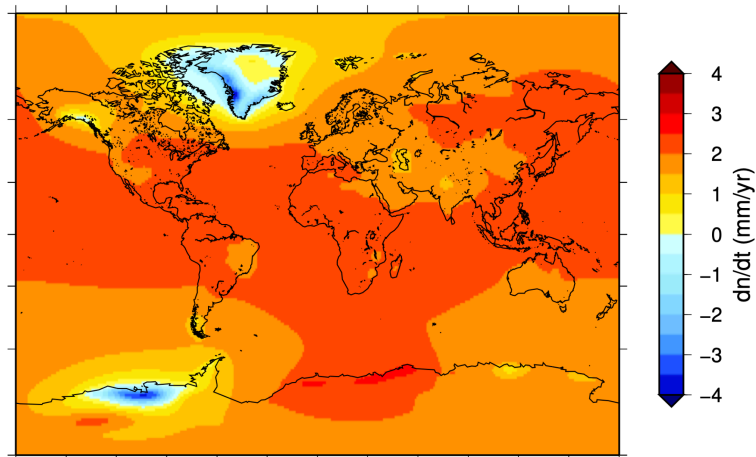


Figure 14: Elastic fingerprints due to trends of present-day mass redistribution on sea surface height change ( $dN/dt$ ). These rates are obtained as a least-squares linear fit of the monthly time series for each field, from April 2002 to December 2019.

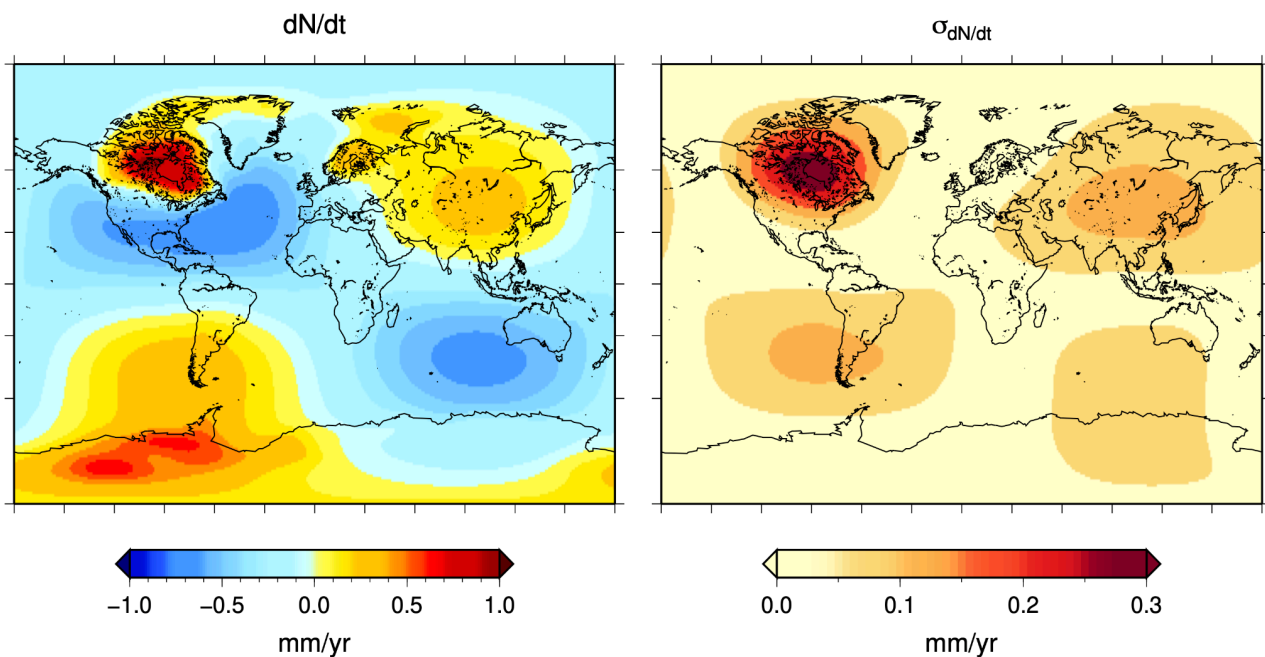


Figure 15: GIA contribution to the present-day rate of absolute sea-level change ( $dN/dt$ , left), according to the ICE-6G (VM5a) model of Argus et al. (2014) and Peltier et al. (2015), implemented into the Sea Level Equation solver SELEN4, and associated uncertainties (right) evaluated as ensemble standard deviations over 20 variations of the VM5a rheological profile. These rates are representative of the time period from April 2002 to December 2019.

## 2.10. Synthetic observations

### 2.10.1. Review of scientific background

Synthetic observations have been extracted from a numerical ocean-sea-ice simulation produced as part of the OCCIPUT project led by T. Penduff (IGE) in collaboration with Jean-Marc Molines (IGE) and S. Leroux (Datlas) (Bessières et al., 2017). OCCIPUT is a global ocean/sea-ice/iceberg simulation that uses the NEMO model, and has a horizontal resolution of  $1/4^\circ$ . It was run as an ensemble experiment (50 members) of which we provide here only the outputs from 1 member (member #1). It ran over the period 1960-2015. The atmospheric forcing applied at the surface comes from the DFS5.2 dataset (Dussin et al., 2016), based on the ERAi reanalysis. It varies over the full range of time-scales from 6 hours to multi-decadal. The freshwater river runoff and icecap melting forcing applied to the experiment is climatological.

### 2.10.2. Selection of used data

#### 2.10.2.1. Altimetric synthetic data

Synthetic observations of along-track SSH have been extracted online during the production of the global, NEMO-based ensemble simulation OCCIPUT (but here we provide the outputs from ensemble member 1), at every single time and locations where a true SLA observation exists in the AVISO database for the along-track altimetry from the Jason-2 satellite continuous series over the period 2009-2015. The model SSH is equivalent to the quantity called anomalous dynamic topography ("ADT") in the usual altimetry terms. The time-mean model SSH of the provided gridded field (see above) can be used as a proxy for the mean dynamic topography ("MDT").

#### 2.10.2.2. Temperature and salinity synthetic data

Synthetic observations of in-situ Temperature and Salinity profiles as a function of depth have been extracted on-line during the production of the global, NEMO-based OCCIPUT simulation at every single time and location (in x,y,z dimensions) where a true in-situ profile exists in the ENACT-3 database (Ingleby and Huddleston, 2007); <https://www.metoffice.gov.uk/hadobs/en3/> over the simulation period: 1961-2015.

#### 2.10.2.3. Gravimetric synthetic data

The gravimetric synthetic dataset is computed using the glaciers mass estimation dataset (Hugonnet et al., 2021), the Antarctica and Greenland ice-sheet mass estimation datasets (Döhne et al., 2023; Groh et al., 2021), the GRACE terrestrial water storage estimation (Blazquez et al., 2018) and the ocean bottom pressure OCCIPUT dataset (Bessières et al., 2017). These datasets are processed to produce a gravimetric synthetic dataset of the temporal mass variation of the Earth between April 2002 and December 2015.



## 2.10.3. Algorithms

### 2.10.3.1. Altimetric synthetic data

The altimetric synthetic dataset is computed as follows:

- The synthetic observations of along-track SSH are concatenated at a monthly time step, then the SSH global mean obtained from OCCIPUT model is read and interpolated at the along track data timestamp.
- The Global Mean Thermosteric Sea Level (GMTSSL) computed from synthetic observations is also interpolated at the along-track data timestamp.
- The Mean Dynamic Topography (MDT) is obtained from computing the time mean of the OCCIPUT ocean model SSH gridded value between the years 1993 and 2017. Then, the MDT is interpolated on a regular grid of  $0.25^\circ$  resolution.
- The SSH global mean is removed from along-track synthetic data, then the GMTSSL is added. This ensures that synthetic altimetric data are coherent with steric synthetic data since SSH global mean has no physical mean (cf Altimetric synthetic data limitations paragraph).
- The MDT is also removed from the along-track synthetic altimetric data because it is a static field that is not necessary for the analysis and which is ever removed from real along-track observations.
- After making these corrections, the along-track synthetic altimetric data are interpolated on a 3 degrees by 1 degree regular grid (following the AVISO procedure). The regular grids are stored at the monthly time step, it does not respect the cycles relative to the altimetry mission it corresponds to.
- Finally, the regular grids are then resampled at a 1 degree resolution using a simple nearest method.

### 2.10.3.2. Steric synthetic data

The synthetic profiles are remapped on a regular  $0.5^\circ \times 0.5^\circ$  grid over 152 standard depths using the ISAS tool (Gaillard et al., 2016). ISAS is based on optimal interpolation (Bretherton et al., 1976), and is designed to map *in-situ* profiles onto a regular grid on a monthly basis to fill the spatio-temporal gaps between missing data and provide an associated error estimate.

The temperature and salinity synthetic profiles are remapped as described in (Llovel et al., 2022) as follows:

- The synthetic temperature and salinity profiles are standardized onto 152 levels.

- A monthly mean and temporal standard deviation climatology of temperature and salinity are generated over the considered time period (i.e. 2005–2015). This climatology consists of a  $5^\circ \times 5^\circ$  binning (mean and variance) of temperature and salinity standardized synthetic profiles for each calendar month. The monthly mean climatology over the period 2005–2015 is used as a first guess for interpolating the monthly ISAS OCCIPUT temperature and salinity gridded fields.
- The annual variance climatology is used as the *a priori* variance for the OI.
- The mapping procedure is applied for each month between January 2005 to December 2015 using different Gaussian weights on an *a priori* variance corresponding to large (300 km) and meso-covariance scales (proportional to the Rossby radius), and unresolved scales.

For steric computation, we use the same algorithm as described in section 2.2.3. However, we first transform the temperature fields into conservative temperature and practical salinity into absolute salinity fields with the TEOS10 equation of sea water.

Thus, steric sea-level anomalies are estimated (Eq.4) by integrating, from the surface to 2000, the density anomalies at each standard level.

$$SSL(x, y, t) = - \frac{1}{\rho_0} \int_{2000}^0 (\rho(T(x, y, z, t), S(x, y, z), p) - \rho_{ref}(0, 35.16504, p)) dz \quad (Eq.4)$$

where  $SSL(x, y, t)$  is the steric sea-level anomaly at location  $x, y$  and time  $t$  (mm),  $\rho_0 = 1026 \text{ kg m}^{-3}$  is the surface seawater density,  $\rho(T(x, y, z, t), S(x, y, z), p)$  is the seawater density ( $\text{kg m}^{-3}$ ) with  $T(x, y, z, t)$  being the conservative temperature ( $^\circ\text{C}$ ),  $S(x, y, z)$  being the absolute salinity and  $p$  being the pressure (dbar).  $\rho_{ref}(0, 35.16504, p)$  is the reference seawater density ( $\text{kg m}^{-3}$ ) where temperature and salinity are constant ( $0^\circ\text{C}$  and  $35.16504 \text{ g/kg}$ , respectively) while the pressure varies. The parameters  $\rho$  and  $\rho_{ref}$  are computed with the GSW toolbox.

#### 2.10.3.3. Gravimetric synthetic data

The gravimetric synthetic dataset is computed as follows:

- The glaciers dataset (Hugonnet et al., 2021) downloaded from <http://dx.doi.org/10.6096/13> (Choose “Download” in the first menu and “Times series” in the second menu, download the “Tile time series” and extract the `dh_world_tiles_1deg_cumul.csv` file). The file is read between April 2002 and December 2015 and converted from gigatonnes to meters of Equivalent Water Height (multiplied by  $10^9$  and divided by the  $1^\circ$  cell surface area). Before the unit conversion, spatial filtering can be applied with a rolling mean window of  $5^\circ$  by  $5^\circ$  (approximately 250 km filtering) to reduce Gibbs effect of the spherical harmonics conversion.

- The Antarctica and Greenland ice-sheets datasets (Döhne et al., 2023; Groh et al., 2021) are downloaded in the form of Gravimetric Mass Balance (GMB) gridded products (50 km by 50 km grid) from [https://data1.geo.tu-dresden.de/ais\\_gmb/](https://data1.geo.tu-dresden.de/ais_gmb/) and [https://data1.geo.tu-dresden.de/gis\\_gmb/](https://data1.geo.tu-dresden.de/gis_gmb/). Both files are read between April 2002 and December 2015 and regridded to 1° by 1° using the Regridder object with the “conservative” option from the Python package xESMF (<https://xesmf.readthedocs.io/en/stable/>). Individual missing months (corresponding to GRACE missing months) are linearly interpolated after removing a trend, an annual cycle and a semi-annual cycle fitted on the time-series. The removed signal is restored after the interpolation.
- The GRACE terrestrial water storage dataset is available on demand to the corresponding author of (Blazquez et al., 2018). The file is read between April 2002 and December 2015 and individual missing months are linearly interpolated after removing a trend, an annual cycle and a semi-annual cycle fitted on the time-series. The removed signal is restored after the interpolation. The mass variations are set to zero over oceans and areas with glaciers, Antarctica and Greenland ice-sheets.
- After processing the sum of the glaciers, ice sheets and terrestrial water storage is computed. The total mass of the sum is uniformly removed over the oceans to ensure mass conservation over time. The resulting product is used to estimate the sea-level fingerprint (Spada and Melini, 2019) on a 1° by 1° grid. The total mass of the sea-level fingerprint is uniformly removed over the oceans to ensure mass conservation over time.
- The ocean bottom pressure OCCIPUT dataset (Bessi eres et al., 2017) is downloaded from <https://ige-meom-opensap.univ-grenoble-alpes.fr/thredds/catalog/meomopensap/extract/M/EOM/OCCIPUT/SHAREDforESA-CCI/gridded-1-day/interp-grid/catalog.html>. The datasets, originally separated into files of one year, are read between April 2002 and December 2015 and daily time-series are converted to a monthly time-series by averaging the values over each month. The data are converted from bar to meters of Equivalent Water Height (divided by the products of the average ocean density of 1030 kg.m<sup>-3</sup>, the mean gravitational acceleration of 9.8065 m.s<sup>-2</sup> and 10<sup>-4</sup>). The total mass of the ocean bottom pressure is uniformly removed over the oceans to ensure mass conservation over time.
- The sum of the sea-level fingerprint and the ocean bottom pressure after processing is converted to spherical harmonics up to degree and order 90. It is then converted to a 1° by 1° grid over the ocean (variable ‘*ocean\_synthetic*’). The same operation is done for the sum of sea-level fingerprint, ocean bottom pressure, glaciers, ice-sheets and terrestrial water storage (variable ‘*gravi\_synthetic*’). The same operation is done for the sum of sea-level fingerprint, ocean bottom pressure, glaciers with spatial filtering, ice-sheets and terrestrial water storage (variable ‘*gravi\_filt\_synthetic*’).

This workflow is represented in operation by operation in the following figure (Fig.16).

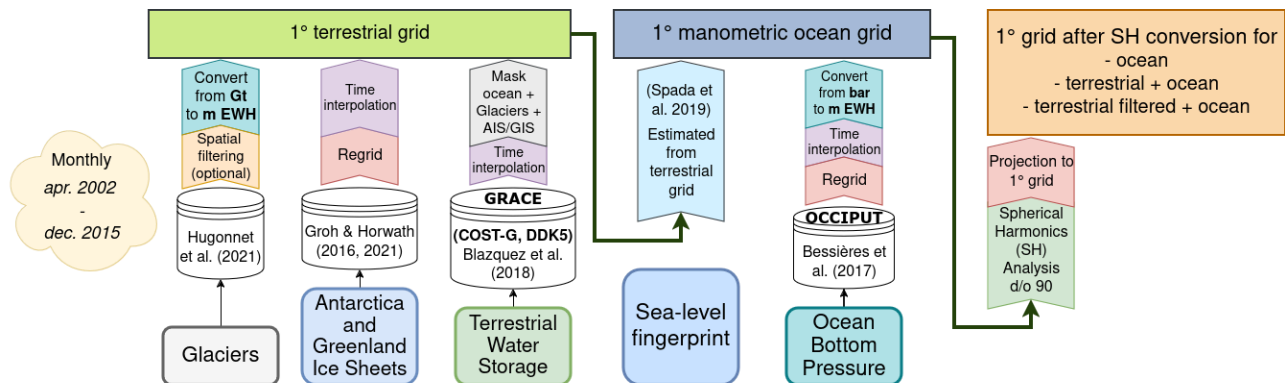


Figure 16: Workflow of the gravimetric synthetic data processing

## 2.10.4. Known limitations

### 2.10.4.1. Altimetric synthetic data

The synthetic observations extracted from the OCCIPUT simulation are, by design, affected by the same limitations as the numerical simulation itself:

- In a Boussinesq model like NEMO, the global mean of SSH has no physical meaning: the global mean of SSH in the model can vary because of the freshwater forcing imbalance  $E - P - R + (SSS \text{ nudging}) - \text{Sea ice}$ . This imbalance of the freshwater fluxes is due to the fact that the different forcing terms are not necessarily consistent with each other: **P** from DFS5.2 reanalysis, **E** derived from forcing surface temperature and humidity and from the ocean model surface state of which the mesoscale features are not necessarily consistent with what the reanalysis atmosphere “saw”, **R** derived from the hydrological reanalysis).
- In the OCCIPUT simulation, the global mean SSH is not controlled on the fly in the model, by resetting the global mean freshwater budget to zero at every timestep. As a consequence, the variations from timestep to timestep of the global mean SSH in OCCIPUT should not be considered as physical and should be removed before analysis. Below we provide SSH gridded fields with the global mean removed.
- In the model, the ocean at rest would be following the geoid (the iso-gravity surface). In the model, the gravity is taken constant ( $9.80665 \text{ m/s}^2$ ) over the globe, which is itself considered a perfect sphere (Radius =  $6371229 \text{ m}$ ).
- In the model in practice, only the SSH gradient is used in the computation of the horizontal surface pressure. SSH is only known to within a constant.
- Note also that the model is driven by a homogeneous and stationary atmospheric surface pressure (set to constant). The atmospheric surface pressure from the atmospheric

reanalysis is only taken into account by the model in the surface flux computation (bulk formulation).

#### 2.10.4.2. Steric synthetic data

No known limitations for the steric synthetic data.

#### 2.10.4.3. Gravimetric synthetic data

The time-series length is limited from April 2002, which corresponds to the GRACE mission beginning, to December 2015, which corresponds to the end of the OCCIPUT simulation run.

The estimation of the spherical harmonics components up to degree and order 90 contains errors due to the spatial resolution of the  $1^\circ$  by  $1^\circ$  grid. This generates Gibbs effects in the transformation to spherical harmonics of the glaciers mass variations, especially for glaciers that are located within a single grid cell. The '*ocean\_synthetic*' estimation does not suffer from this limitation, but the '*gravi\_synthetic*' estimation where the glaciers component is not spatially filtered, suffers major Gibbs effects near the Alaska and Andes regions.

The dataset is delivered on a  $1^\circ$  by  $1^\circ$  grid, but its effective spatial resolution due to the conversion into the spherical harmonics up to degree and order 90 is approximately 220 km.

## 3. Sea level budget computation chain

### 3.1. Overview

This section details the main algorithms that will be used to compute the Sea Level Budget (SLB) and its residuals by using the "Input data" detailed in paragraph 2. This section is divided into 2 parts, the first one is relative to the computation of the SLB with the "classical approach" developed in the first phase of the SLBC\_cci project (Horwath et al., 2022). It will consist in updating the SLB using as input the sea level components selected and the associated uncertainties. The second part will consist in providing an objective solution of the SLB with a combination of sea level components that is optimally determined to close as much as possible the SLB within uncertainties of each SLB component.

### 3.2. Input data

We use the following notations for input components:

*Table 5: Table describing the input data used in the sea level budget and ocean mass budget equations*

Notation	Name	Description
----------	------	-------------

$\Delta SL_{abs}$	Absolute sea level changes	absolute sea level changes, or the sea surface height relative to the reference ellipsoid, sometimes referred to as $N$ . Satellite altimetry products estimate absolute sea level changes, so that $(\Delta SL_{abs})_{alti} = \Delta SL_{abs} + \epsilon_{alti}$ , where $\epsilon_{alti}$ is the error in the measurement of absolute sea level changes by satellite altimetry, due to errors in the orbit, range measurement, WTC, but excluding GIA.
$\Delta SL_{rel}$	Relative sea level changes	relative sea level changes, which are the changes in the total water height from the surface to the seafloor, sometimes referred to as $S$ . Relative sea level changes are the difference between absolute sea level changes and vertical land motions :  $\Delta SL_{rel} = (\Delta SL_{abs})_{alti} - \Delta VLM + \epsilon_{alti}$
$\Delta VLM$	Vertical land motions	the vertical land motions, or the changes in the height of the seafloor relative to the reference ellipsoid, in this document expressed as $\Delta VLM = N_{GIA} + \Delta VLM_{current}$ , where the GIA correction for altimetry, noted $N_{GIA} = S_{GIA} + U_{GIA}$ , includes a correction for the geoid and vertical land motion. GIA affects all the components of the sea level equation, not only the vertical land motion. Therefore, when correcting altimetry for GIA it is important to use $N_{GIA}$ and not $U_{GIA}$ . $\Delta VLM_{current}$ are all sources of vertical land motions not due to GIA. In practice, we can go a step further and separate all other sources of vertical land motions in a contribution from Present-Day Ice Melting (PDIM) and some residual errors such as $\Delta VLM_{current} = \Delta VLM_{PDIM} + \epsilon_{VLM}$ . Note that here we consider $\Delta VLM = N_{GIA} + \Delta VLM_{PDIM} + \epsilon_{VLM} + \epsilon_{NGIA}$ , where $\epsilon_{NGIA}$ are the errors on the GIA correction for absolute sea level changes.
$\Delta SL_{thermo}$	Thermosteric	thermosteric sea level change from in-situ data
$\Delta SL_{halo}$	Halosteric	halosteric sea level change from in-situ data

$\Delta SL_{steric} = \Delta SL_{thermo} + \Delta SL_{halo}$	Steric	steric sea level change, knowing that $(\Delta SL_{steric})_{insitu} = \Delta SL_{steric} + \epsilon_{insitu}$ where $(\Delta SL_{steric})_{insitu}$ , are the estimates of steric sea level changes based on in situ data and $\epsilon_{insitu}$ are the errors in the estimation of steric sea level changes by in situ temperature and salinity measurements.
$\Delta SL_{manGIA}$	Manometric sea level change from gravimetric data excluding the effect of GIA	manometric sea level change from gravimetric data excluding the effect of GIA on manometric sea level and including the manometric effect of land ice, land water and atmospheric water content components. In practice we do not know perfectly the manometric component, we can consider that the satellite gravimetry measurements of manometric sea level changes including all necessary corrections for sources of geophysical signal measured by the GRACE and GRACE-FO but not related to changes in the ocean mass (i.e. GIA, earthquakes, atmosphere, etc.) is expressed as $(\Delta SL_{manGIA})_{gravi} = \Delta SL_{manGIA} + \epsilon_{gravi}$ , with $\epsilon_{gravi}$ are the errors in the measurement of manometric sea level changes by GRACE and GRACE-FO missions, including instrumental errors, background model errors, and post-processing errors.
$\Delta GMSL_{abs}$	Global mean absolute sea level	global mean absolute sea level from altimetry data (i.e. weighted global mean of $\Delta SL_{abs}$ ).
$\Delta GMSL_{rel}$	Global mean relative sea level	global mean relative sea level from altimetry data (i.e. weighted global mean of $\Delta SL_{rel}$ ).
$\Delta GMSL_{thermo}$	Global mean thermosteric	global mean thermosteric sea level (i.e. weighted global mean of $\Delta SL_{thermo}$ ).
$(\Delta GMSL_{bary})_{sat}$	Barystatic	barystatic sea level change from gravimetric data (i.e. weighted global mean of $\Delta SL_{manGIA}$ )



$\Delta GMVLM = GMN_{GIA} + \Delta GMVLM_{current}$	Global mean vertical land motions	global mean vertical land motions, or the changes in the height of the seafloor relative to the reference ellipsoid
$(\Delta GMSSL_{bary})_{GIS}$	Greenland ice-sheet	Greenland ice-sheet contribution to barystatic sea level change
$(\Delta GMSSL_{bary})_{AIS}$	Antarctica ice-sheet	Antarctica ice-sheet contribution to barystatic sea level change
$(\Delta GMSSL_{bary})_{GIC}$	Land glaciers and ice-cap	land glaciers and ice-cap contribution to barystatic sea level change
$(\Delta GMSSL_{bary})_{LWS}$	Land water storage	land water storage contribution to barystatic sea level change
$(\Delta GMSSL_{bary})_{WV}$	Atmosphere water vapour	atmosphere water vapour contribution to barystatic sea level change

### 3.3. Sea level budget and Ocean mass budget equations

We use the following notations for the sums of components:

- Sum of the barystatic component from gravimetry and of the thermosteric component from in-situ data:

$$\Delta GMSSL_{abs} = \Delta GMSSL_{bary} + \Delta GMSSL_{thermo} + \Delta GMVLM \quad (Eq.5)$$

- Barystatic sea level change from the sum of individual ocean mass contributions:

$$\begin{aligned} (\Delta GMSSL_{bary})_{sum} = & (\Delta GMSSL_{bary})_{GIS} + (\Delta GMSSL_{bary})_{AIS} \\ & + (\Delta GMSSL_{bary})_{GIC} + (\Delta GMSSL_{bary})_{LWS} + (\Delta GMSSL_{bary})_{WV} \end{aligned} \quad (Eq.6)$$

We use the following notations for the budget residuals:

- $r$  and  $R$ : residuals of the local sea level and global mean sea level budgets, respectively, using altimetry, gravimetric and in-situ data.
- $S$ : residuals of the global mean ocean mass budget using gravimetric data and individual ocean mass contributions

- $T$ : residuals of the global mean sea level budget using altimetry and in-situ data and individual ocean mass contributions (without GRACE)

## 3.4. Algorithms

### 3.4.1. Unconstrained approach: Historical approach

#### 3.4.1.1. Computation of the sea level budget residuals

The sea level budget residuals  $r$  are computed from the sea level budget components as follows:

$$r = (\Delta SL_{abs})_{alti} - (\Delta SL_{man_{GIA}})_{gravi} - (\Delta SL_{steric})_{insitu} - \Delta VLM_{current} - N_{GIA} \quad (Eq.7)$$

(which can be simplified as:  $r = \Delta SL_{rel} - (\Delta SL_{man_{GIA}})_{gravi} - (\Delta SL_{steric})_{insitu}$ ).

In Eq.7, all variables have three dimensions, namely longitude, latitude and time.

#### 3.4.1.2. Computation of the global mean sea level budget residuals

From gridded datasets, the global mean components are computed by weighted averages of the component over the oceans, weighting by the cell surface area and by the water-to-land ratio, and applying a common mask. In this section, all variables have one dimension: time.

The global mean sea level budget residuals  $R$  are computed from the global mean components as follows:

$$R = \Delta GMSL_{rel} - \Delta GMSL_{bary} - \Delta GMSL_{thermo}. \quad (Eq.8)$$

In global mean, the halosteric sea level is negligible (Gregory and Lowe, 2000; Llovel et al., 2019). Considering only the thermosteric component avoids including halosteric data with spurious drifts (Barnoud et al., 2021).

The global mean ocean mass budget residuals  $S$  are computed from the barystatic component from GRACE and the individual mass contributions to sea level change as:

$$S = (\Delta GMSL_{bary})_{sat} - (\Delta GMSL_{bary})_{GIS} - (\Delta GMSL_{bary})_{AIS} \\ - (\Delta GMSL_{bary})_{GIC} - (\Delta GMSL_{bary})_{LWS} - (\Delta GMSL_{bary})_{WV} \quad (Eq.9)$$

The global mean sea level budget residuals  $T$  can also be computed by replacing the GRACE estimate of the barystatic component by the sum of the individual contributions to ocean mass change as follows:

$$T = \Delta GMSL_{rel} - \Delta GMSL_{thermo} - (\Delta GMSL_{bary})_{GIS} - (\Delta GMSL_{bary})_{AIS} - (\Delta GMSL_{bary})_{GIC} - (\Delta GMSL_{bary})_{LWS} - (\Delta GMSL_{bary})_{WV} \quad (Eq.10)$$

Note that these three budget equations (Eq.8, Eq.9 and Eq.10) are not independent as any of these equations is the sum or the difference of the other two equations. Only two of these equations are sufficient to fully describe the sea level and ocean mass budgets.

The covariance matrix of the residuals is simply the sum of the covariance matrices of each component involved in the budget. For instance, for the global mean sea level (Eq.8), the covariance matrix of the residuals  $C_R$  is given by:

$$C_R = C_{GMSL_{rel}} + C_{GMSL_{bary}} + C_{GMSL_{thermo}}, \quad (Eq.11)$$

where  $C_{GMSL_{abs}}$  is the covariance matrix of the altimetry-based global mean sea level,  $C_{GMSL_{bary}}$  is the covariance matrix of the gravimetry-based barystatic sea level and  $C_{GMSL_{thermo}}$  is the covariance matrix of the in situ-based global mean thermosteric sea level.

### 3.4.2. Constrained approach: Innovative approach

Given the observed components listed in the input data section (section 3.2) and knowing that the budget residuals are physically supposed to be null, this section presents how the components are inverted to get an estimate of optimal components of sea level change. The method followed is based on the approach of (Rodell et al., 2015) for the water cycle and of (L'Ecuyer et al., 2015) for the energy budget.

#### 3.4.2.1. Estimation of global mean components

Let's define the vector  $m$  containing the relative sea level, barystatic and thermosteric components:

$$\mathbf{m} = \begin{bmatrix} GMSL_{rel}(1) \\ \vdots \\ GMSL_{rel}(nt) \\ GMSL_{bary}(1) \\ \vdots \\ GMSL_{bary}(nt) \\ GMSL_{thermo}(1) \\ \vdots \\ GMSL_{thermo}(nt) \end{bmatrix} \quad (Eq.12)$$

where  $nt$  is the number of time samples.

We note  $\mathbf{m}_{obs}$  the vector containing the observed components and  $\mathbf{m}_{est}$  the vector containing the estimated components.

The covariance matrix of the observed component vector  $\mathbf{C}_{obs}$  is a  $[3nt, 3nt]$  block diagonal matrix containing the  $[nt, nt]$  covariance matrices of each component on the diagonal blocks:

$$\mathbf{C}_{obs} = \begin{bmatrix} \mathbf{C}_{GMSL_{alti}} & 0 & 0 \\ 0 & \mathbf{C}_{GMSL_{bary}} & 0 \\ 0 & 0 & \mathbf{C}_{GMSL_{thermo}} \end{bmatrix}. \quad (Eq.13)$$

We also define the vector of the global mean sea level budget residuals as:

$$\mathbf{R} = \begin{bmatrix} R_1 \\ \vdots \\ R_{nt} \end{bmatrix} \quad (Eq.14)$$

The component vector and the residual vector are linearly related via the Jacobian matrix  $\mathbf{K}$  containing the derivatives of  $\mathbf{R}$  with respect to  $\mathbf{m}$ :

$$\mathbf{R} = \mathbf{K}\mathbf{m} \quad (Eq.15)$$

where  $\mathbf{K}$  is a  $[nt, 3nt]$  matrix constructed as follows:

$$\mathbf{K} = \begin{bmatrix} 1 & 0 & \dots & 0 & -1 & 0 & \dots & 0 & -1 & 0 & \dots & 0 \\ 0 & \ddots & & \vdots & 0 & \ddots & & \vdots & 0 & \ddots & & \vdots \\ \vdots & & \ddots & \vdots & \vdots & & \ddots & \vdots & \vdots & & \ddots & \vdots \\ 0 & \dots & 0 & 1 & 0 & \dots & 0 & -1 & 0 & \dots & 0 & -1 \end{bmatrix} = [\mathbf{I}_{nt} \quad -\mathbf{I}_{nt} \quad -\mathbf{I}_{nt}] \quad (\text{Eq.16})$$

where  $\mathbf{I}_{nt}$  is the identity matrix of dimension  $[nt, nt]$ .

The cost function  $J$  includes one term to minimise the likelihood of the components given their covariance matrix and one term to minimise the residuals computed from the estimated components as they should be null:

$$J(\mathbf{m}) = ||\mathbf{m} - \mathbf{m}_{\text{obs}}||^2 + \alpha ||\mathbf{R}||^2 = (\mathbf{m} - \mathbf{m}_{\text{obs}})^T \mathbf{C}_{\text{obs}} (\mathbf{m} - \mathbf{m}_{\text{obs}}) + \alpha (\mathbf{K}\mathbf{m})^T \quad (\text{Eq.17})$$

The scalar  $\alpha$  is a trade-off coefficient between the two terms to minimise. It can be set to 1, determined empirically or optimally determined by methods such as leave-one-out or cross-validation sum of squares. In the following, we arbitrarily consider  $\alpha = 1$ .

The model  $\mathbf{m}_{\text{est}}$  minimising the cost function  $J$  is expressed as (Rodell et al., 2015):

$$\mathbf{m}_{\text{est}} = \mathbf{m}_{\text{obs}} - (\mathbf{K}^T \mathbf{K} + \mathbf{C}_{\text{obs}}^{-1})^{-1} \mathbf{K}^T \mathbf{K} \mathbf{m}_{\text{obs}} \quad (\text{Eq.18})$$

And its associated covariance matrix is:

$$\mathbf{C}_{\text{est}} = (\mathbf{K}^T \mathbf{K} + \mathbf{C}_{\text{obs}}^{-1})^{-1} \quad (\text{Eq.19})$$

#### 3.4.2.2. Estimation of global mean components with ocean mass balance estimates

Similarly to the inversion with barystatic sea level measured by gravimetry, it is possible to perform an inversion by using the ocean mass balance budget where the barystatic sea level is estimated from the individual mass components (Antarctica, Greenland, glaciers, etc...).

There is then 2 different systems that can be expressed and inverted simultaneously (Eq.8 and Eq.9)

We can therefore express the vector  $\mathbf{m}$  containing the relative sea level, individual mass component and thermosteric components:

$$\mathbf{m} = \begin{bmatrix} GMSL_{abs}(1) \\ \vdots \\ GMSL_{abs}(nt) \\ GMSL_{bary}(1) \\ \vdots \\ GMSL_{bary}(nt) \\ GMSL_{thermo}(1) \\ \vdots \\ GMSL_{thermo}(nt) \\ (GMSL_{bary})_{AIS}(1) \\ \vdots \\ (GMSL_{bary})_{AIS}(nt) \\ (GMSL_{bary})_{GIS}(1) \\ \vdots \\ (GMSL_{bary})_{GIS}(nt) \\ (GMSL_{bary})_{GIC}(1) \\ \vdots \\ (GMSL_{bary})_{GIC}(nt) \\ \vdots \end{bmatrix} \quad (Eq.20)$$

We also define the vector of the global mean sea level budget and ocean mass budget residuals as:

$$\mathbf{R} = \begin{bmatrix} R_1 \\ \vdots \\ R_{nt} \\ S_1 \\ \vdots \\ S_{nt} \end{bmatrix} \quad (Eq.21)$$

The component vector and the residual vector are linearly related via the Jacobian matrix  $\mathbf{K}$  containing the derivatives of  $\mathbf{R}$  with respect to  $\mathbf{m}$ . Where  $\mathbf{K}$  is a  $[2nt, 8nt]$  matrix constructed as follows:

$$\mathbf{K} = \begin{bmatrix} \mathbf{I}_{nt} & -\mathbf{I}_{nt} & -\mathbf{I}_{nt} & 0 & 0 & 0 & 0 & 0 \\ 0 & \mathbf{I}_{nt} & 0 & -\mathbf{I}_{nt} & -\mathbf{I}_{nt} & -\mathbf{I}_{nt} & -\mathbf{I}_{nt} & -\mathbf{I}_{nt} \end{bmatrix} \quad (Eq.22)$$

Then the cost function and the results of the inverse method are the same as presented in Eq.17, Eq.18, Eq.19.

#### 3.4.2.3. Estimation of local sea level budget components

As there are no spatial correlations for any component of the sea level budget, the local sea level budget components can be estimated similarly by solving the inversion for the time series at each cell independently, adding the halosteric sea level change in the component vector as the halosteric contribution is not negligible locally.

### 3.5. Known limitations

The reliability of the estimated components rely on the robustness and fairness of estimated covariance matrices of all components. If the uncertainties of a component are overestimated while the uncertainties of another component are underestimated, the inversion result will not be reliable. Sensitivity tests will be performed to evaluate the impact of this limitation on the inversion results.



**END OF DOCUMENT**